JGR Solid Earth

RESEARCH ARTICLE
10.1029/2019JB019239

Key Points:
- Average and interval *Vp*/*Vs* versus depth functions derived from *S*-converted waves from the Ridge-to-Trench seismic experiment in Cascadia Basin
- Layers with high *Vp*/*Vs* indicate elevated pore fluid pressure in incoming sediments
- Variations in *Vp*/*Vs* structure correlate with underthrust sediment thickness and wedge deformation style

Supporting Information:
- Supporting Information S1

Correspondence to:
J. P. Canales,
jpcanales@whoi.edu

Citation:
Zhu, J., Canales, J. P., Han, S., Carbotte, S. M., Arnulf, A., & Nedimović, M. R. (2020). *Vp*/*Vs* ratio of incoming sediments off Cascadia subduction zone from analysis of controlled-source multicomponent OBS records. *Journal of Geophysical Research: Solid Earth*, *125*, e2019JB019239. https://doi.org/10.1029/2019JB019239

Received 13 DEC 2019
Accepted 19 MAY 2020
Accepted article online 28 MAY 2020

Vp/*Vs* Ratio of Incoming Sediments Off Cascadia Subduction Zone From Analysis of Controlled-Source Multicomponent OBS Records

Jian Zhu[1], J. Pablo Canales[1], Shuoshuo Han[2], Suzanne M. Carbotte[3], Adrien Arnulf[2], and Mladen R. Nedimović[4]

[1]Department of Geology and Geophysics, Woods Hole Oceanographic Institution, Woods Hole, MA, USA, [2]Institute for Geophysics, Jackson School of Geosciences, University of Texas at Austin, Austin, TX, USA, [3]Lamont-Doherty Earth Observatory, Columbia University, Palisades, NY, USA, [4]Department of Earth Sciences, Dalhousie University, Halifax, Nova Scotia, Canada

Abstract *P*-to-*S*-converted waves observed in controlled-source multicomponent ocean bottom seismometer (OBS) records were used to derive the *Vp*/*Vs* structure of Cascadia Basin sediments. We used *P*-to-*S* waves converted at the basement to derive an empirical function describing the average *Vp*/*Vs* of Cascadia sediments as a function of sediment thickness. We derived one-dimensional interval *Vp*/*Vs* functions from semblance velocity analysis of *S*-converted intrasediment and basement reflections, which we used to define an empirical *Vp*/*Vs* versus burial depth compaction trend. We find that seaward from the Cascadia deformation front, *Vp*/*Vs* structure offshore northern Oregon and Washington shows little variability along strike, while the structure of incoming sediments offshore central Oregon is more heterogeneous and includes intermediate-to-deep sediment layers of anomalously elevated *Vp*/*Vs*. These zones with elevated *Vp*/*Vs* are likely due to elevated pore fluid pressures, although layers of high sand content intercalated within a more clayey sedimentary sequence, and/or a higher content of coarser-grained clay minerals relative to finer-grained smectite could be contributing factors. We find that the proto-décollement offshore central Oregon develops within the incoming sediments at a low-permeability boundary that traps fluids in a stratigraphic level where fluid overpressure exceeds 50% of the differential pressure between the hydrostatic pressure and the lithostatic pressure. Incoming sediments with the highest estimated fluid overpressures occur offshore central Oregon where deformation of the accretionary prism is seaward vergent. Conversely, landward vergence offshore northern Oregon and Washington correlates with more moderate pore pressures and laterally homogeneous *Vp*/*Vs* functions of Cascadia Basin sediments.

1. Introduction

At subduction zones, incoming sediment composition and physical properties influence décollement development and are one of the factors controlling the up-dip extent of megathrust rupture, including the potential for tsunamigenic slip to the trench (Dean et al., 2010; Geersen et al., 2013; Gulick et al., 2011; Han et al., 2017; Hüpers et al., 2017; Vannucchi et al., 2017). The increasing temperatures at the basement, caused by landward thickening of incoming sediments acting as a thermal blanket, alter the deep sediment composition and properties by triggering mineral transformation, dehydration, and lithification prior to subduction (Geersen et al., 2013). Also, large-magnitude earthquakes occur preferentially where thick incoming sediments contribute to a smooth plate interface, which favors rupture propagation over long distances (Heuret et al., 2012; Scholl et al., 2015; Seno, 2017; van Rijsingen et al., 2018).

At Cascadia no great subduction zone earthquakes have been instrumentally recorded (McCrory et al., 2012; Tréhu et al., 2008, 2015), but paleoseismic studies show that great megathrust earthquakes (Mw ≥ 8) have occurred during the Holocene with intervals of 200–530 years (Atwater, 1987; Atwater & Hemphill-Haley, 1997; Goldfinger et al., 2003, 2017). Here, the heavily sedimented incoming Juan de Fuca, Explorer, and Gorda plates (hereinafter collectively called Juan de Fuca plate system) (e.g., Gulick et al., 1998; Han et al., 2016; MacKay, 1995; Nedimović et al., 2008) subduct obliquely beneath North America (Atwater, 1970; Wilson, 2002). Some direct information on incoming composition of the sediment section, which can generally be described as abyssal plain turbidites and Astoria and Nitinat Fan deposits, and

other physical properties at the Cascadia margin is available from drilling observations: DSDP Leg 18 Site 174 (Shipboard Scientific Party, 1973), ODP Leg 146 Sites 888–892 (Shipboard Scientific Party, 1994; Westbrook et al., 1994), ODP Leg 168 Sites 1,023–1,032 (Fisher & Davis, 1997; Shipboard Scientific Party, 1997b), and ODP Leg 204 Sites 1,044–1,052 (Shipboard Scientific Party, 2003) (Figure 1). Physical properties estimated from indirect geophysical methods, such as *P* wave velocity (*Vp*) derived from multichannel seismic (MCS) data, have also provided important information on sediment consolidation, pore fluid expulsion, and physical properties of the décollement (Cochrane et al., 1994; Han et al., 2017; Yuan et al., 1994).

In addition to *Vp*, the sensitivity of *S* wave velocity (*Vs*) and *Vp*/*Vs* ratio to mineralogy, fluid content, stress state, and fluid overpressures (e.g., Blangy et al., 1993; Castagna et al., 1985; Dvorkin et al., 1999; Lee, 2003; Prasad, 2002; Zimmer et al., 2002) make these parameters very useful for constraining the porosity, consolidation state, presence of elevated pore fluid pressures, and distribution and alignment of cracks in sediments at subduction zones (Peacock & Westbrook, 2000; Peacock et al., 2010; Tsuji et al., 2011, 2014). In this study, we present quantitative analyses of the *Vp*/*Vs* structure of Cascadia Basin sediments using *P*-to-*S*-converted waves observed in controlled-source multicomponent ocean bottom seismometer (OBS) data acquired as part of the 2012 Ridge-to-Trench experiment (Canales & Carbotte, 2012; Carbotte et al., 2014). Previous studies using these data sets reported *Vp* structure, thickness, and reflectivity of sediment, crustal layers, and upper mantle across the full span of the Juan de Fuca plate and along ~350 km of the Cascadia deformation front (CDF) (Canales et al., 2017; Han et al., 2016, 2017, 2018; Horning et al., 2016). Our new results build upon these studies and provide new information on the *Vp*/*Vs* structure of Cascadia Basin sediments from near the Juan de Fuca Ridge to the CDF and on the regional along-strike variability in sediment *Vp*/*Vs* structure along the CDF, with implications for proto-décollement development and style of wedge deformation.

2. Geological Background

Cascadia subduction zone extends over 1,000 km from the Mendocino triple junction in northern California, along the Oregon and Washington continental margin, to north of Vancouver Island (e.g., McCrory et al., 2012), where the Juan de Fuca plate system subducts obliquely beneath continental North America in a direction of N68°E (Wilson, 2002) (Figure 1). The east-northeastward subduction rate is variable along strike, increasing from 30 mm/year off northern California to 45 mm/year off northern Washington and central Vancouver Island and from there decreasing to less than 20 mm/year off northern Vancouver Island (e.g., Wilson, 2002). The Juan de Fuca plate system is covered by Cascadia Basin sediments that thicken rapidly toward the continental margin, reaching a thickness of 1.8–3.1 km over the 5- to 9-Myr-old Juan de Fuca plate (Wilson, 2002) at the onset of subduction along the CDF offshore Washington and Oregon (e.g., Adam et al., 2004; Canales et al., 2017; Han et al., 2017, 2018; MacKay, 1995; Nedimović et al., 2008) and up to 3.5 km at the CDF over the ~5- to 6.5-Myr-old Gorda plate off northern California (Gulick et al., 1998). Deep drilling has revealed a history of rapid accumulation of hemipelagic sediments, turbidites, glacial deposits, and submarine fans since the Pliocene (e.g., Davis et al., 1992; Goldfinger et al., 2012; Johnson et al., 2012). Sediment lithostratigraphy on 3.6-Myr-old crust (ODP Site 1,027, ~100 km seaward of the deformation front off northern Washington, Figure 1) consists of a unit of Quaternary hemipelagic mud (clayey silt to silty clays) and turbidites (silt-to-sandy silts and sands) (0–184 m below seafloor [mbsf]), Late Pleistocene silt turbidites intercalated with hemipelagic mud (silty clay-to-clayey silts) (184–467 mbsf), and Late Pliocene hemipelagic mud with gradually increasing degree of induration with depth to lithified mudstones (467–569 mbsf) over basaltic basement (Shipboard Scientific Party, 1997a). Closer to the deformation front on ~8-Myr-old crust (DSDP Site 174, ~75 km seaward of the deformation front off central Oregon, Figure 1), sediments consist of Upper Pleistocene turbidite sands (69%) and to a lesser extent silty clays and silts over the base of the Astoria Fan (0–284 mbsf) and Upper-to-Lower Pleistocene and Pliocene silt and silty clays and very rarely fine sands (284–879 mbsf) (the deepest sediments at 879–911 mbsf overlaying basement were not penetrated at this site) (Shipboard Scientific Party, 1973). Near the deformation front on ~6.5-Myr-old crust (ODP Site 888, 7 km seaward of the deformation front on the Nitinat Fan off southern Vancouver Island/northern Washington, Figure 1), sediments consist of Holocene-Upper Pleistocene clayey silts and sands (0–193 mbsf), Upper Pleistocene fine-to-medium grained sands (193–457 mbsf), and Upper Pleistocene clayey silts and silts showing incipient lithification and glacial dropstones at the bottom of the

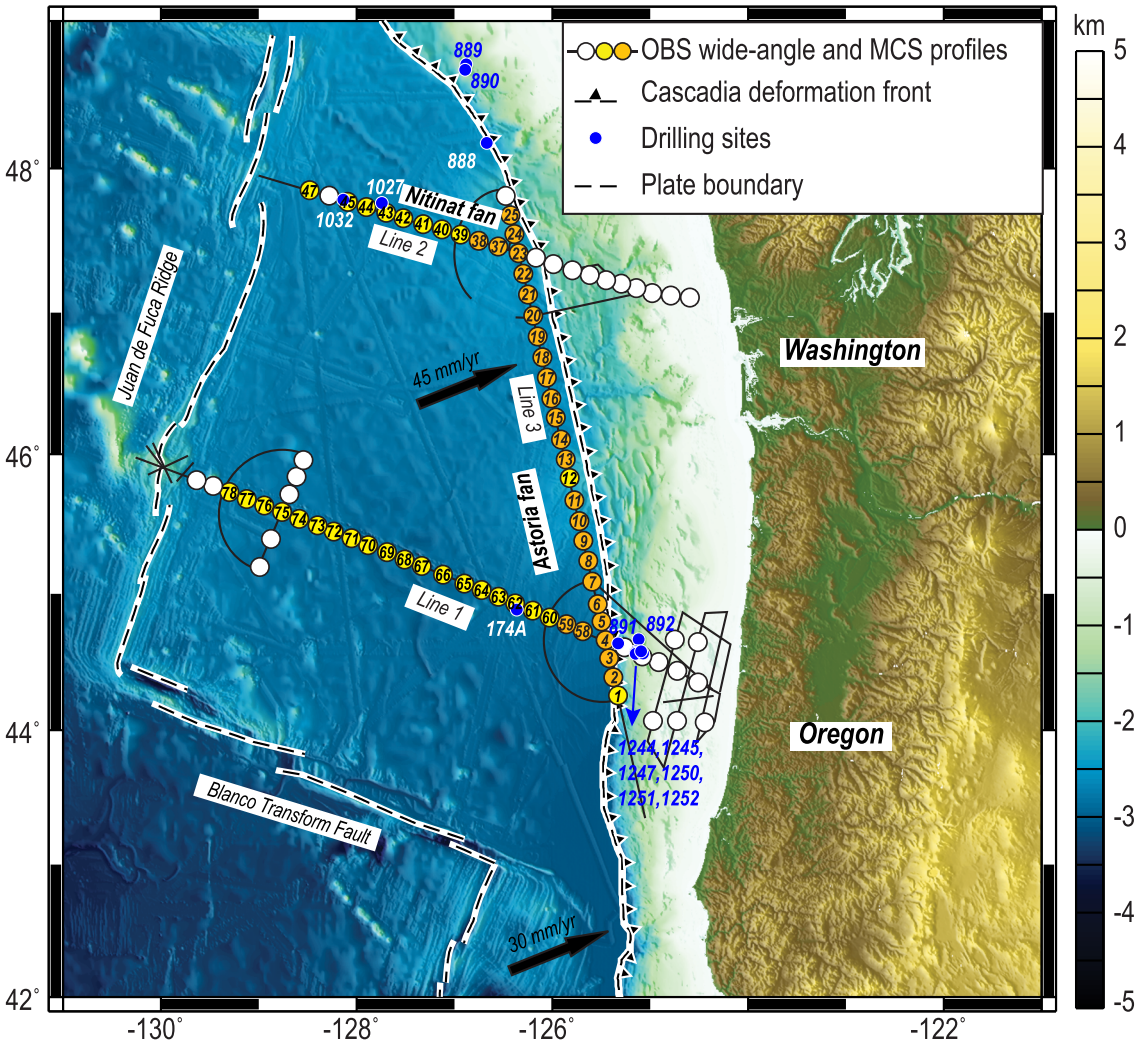

Figure 1. Bathymetric map of Juan de Fuca plate and US continental margin off Oregon and Washington. Black dashed lines indicate the plate boundaries, and dashed line with triangles marks the toe of the Cascadia deformation front. Circles represent OBSs deployed during the 2012 Ridge-to-Trench experiment. OBSs used in this study are numbered: yellow symbols for sites used for calculating average *Vp*/*Vs* ratios and orange symbols for sites used for computing intrasediment interval *Vp*/*Vs* ratios. Solid black lines are multichannel seismic and wide-angle shooting lines. Blue circles are DSDP and ODP drilling sites.

unit (457–567 m). Here porosity and shear strength measurements in cored sediments indicate that sediments in the upper 457 m are underconsolidated, probably due to rapid deposition (the deepest sediments at 600–2,500 mbsf overlaying basement were not penetrated at this site) (Shipboard Scientific Party, 1994).

At the subduction front, most of the sediments on the Juan de Fuca plate system are accreting to the margin forming an active accretionary prism. Deformation of the Cascadia margin is well illustrated by fold and thrust belts of the accretionary prism, which are in general subparallel to the margin in response to the normal component of plate convergence (Carson et al., 1974; Goldfinger et al., 1991, 1992; MacKay et al., 1992; McNeill et al., 2000; Silver, 1972). The CDF is characterized by variable structural vergence. Thrust faults are seaward vergent offshore central Oregon, as well as in some areas off northern California and north of 48°07′ N off Vancouver Island (e.g., Davis & Hyndman, 1989; Gulick et al., 1998; Hyndman et al., 1990; Spence et al., 2001). Vergence off southern Oregon is not well constrained. In contrast, thrust faults appear to be landward vergent in parts of the northern California wedge and on the northern Oregon and Washington margins between 44°55′ and 48°07′N (Adam et al., 2004; Flueh et al., 1998; Gulick et al., 1998; MacKay, 1995; MacKay et al., 1992). The landward vergence has been proposed to result from low shear

stress of the basal décollement, elevated pore pressures due to high sedimentation rates, mechanically strong wedge, the curvature of the margin, and/or along-strike variations in sediment composition and physical properties (Adam et al., 2004; Gutscher et al., 2001; MacKay, 1995).

In the vicinity of the CDF, seismic velocities of incoming sediments increase, and porosities decrease landward as a result of sediment consolidation due to horizontal compression, with ~1/3 of incoming pore fluid content estimated to be lost by the time of sediment accretion to the wedge (Yuan et al., 1994). The thickness of subducted sediments varies along strike: the décollement develops just above basement offshore Washington, <0.6 km above basement between 45°50′ and 47°15′N and 1.4–1.7 km above basement between 44°30′ and 44°50′N, with limited data constraints further south (Adam et al., 2004; Booth-Rea et al., 2008; Han et al., 2016, 2017; MacKay, 1995). This variability in décollement depth may result from along-strike variations in incoming sediment consolidation, as inferred from *Vp* models derived through prestack depth migration of MCS data (Han et al., 2017). Cochrane et al. (1994) suggest that the proto-décollement offshore central Oregon is associated with a reversal in *Vp* resulting from increased porosity due to overpressured pore fluids trapped by low-permeability sediments above the proto-décollement. Han et al. (2017) hypothesize that the presence/absence of layers with intrinsic frictional weakness or low permeability in the sediment sections and/or seamount subduction may all play a role in determining the lower consolidation state of the basal sediments and facilitating development of the proto-décollement.

3. Data Acquisition and Processing

We use controlled-source seismic data recorded by 56 OBSs deployed along three transects (Lines 1, 2, and 3, Figure 1) as part of the Ridge-to-Trench experiment (Table 1). The short-period OBSs were equipped with three-component (one vertical and two horizontal) 4.5-Hz geophones and a hydrophone. The OBSs recorded acoustic signals from the R/V M. Langseth 6,600-cu.in. airgun array at a sampling rate of 200 Hz. The airgun array was triggered along the three profiles in two different configurations: every 37.5 m for MCS profiling (Han et al., 2016, 2018) and every 500 m for a wide-angle survey (Canales et al., 2017; Horning et al., 2016). All of the OBSs recorded the wide-angle shots, and many of the OBSs also recorded a significant portion of the MCS shots along the OBS profiles.

P wave refractions and reflections from the sediments, crust, and mantle are clearly recorded in the vertical and hydrophone components (Canales et al., 2017; Horning et al., 2016). In addition, the horizontal components are rich in high-quality *S*-converted waves. The most prominent *S* wave arrivals are *P*-to-*S* conversions at the crust-sediment interface of up-going *P* waves (crustal and mantle phases) (*PPS*) as well as *S*-converted reflections (down-going *P* reflected upward as *S*) P_iS, where *i* denotes the reflecting interface (basement or intrasediment reflectors) (Figure 2). *PPS* modes were recognized in early seismic studies of ocean crust (Au & Clowes, 1984; Spudich & Orcutt, 1980) and have been used since in a number of studies to investigate the *Vs* and *Vp*/*Vs* (or Poisson's ratio) structure of marine sediments (e.g., Au & Clowes, 1984; Contreras-Reyes et al., 2008; Fujie et al., 2013; Tsuji et al., 2011). P_iS modes, known as *C* waves (e.g., Stewart et al., 2003; Thomsen, 1999), are commonly used in seismic reflection imaging for hydrocarbon exploration and have also been observed and used in numerous studies and diverse tectonic settings, including convergent margins (e.g., Dash & Spence, 2011; Eccles et al., 2009; Peacock et al., 2010; Westbrook et al., 2008). Seismic phases used in this study (Figure 2a) include direct water arrivals (P_{water}), *P* wave crustal refractions (P_g), and *PPS* modes observed in the receiver gathers of the wide-angle shots and P_iS modes observed in the spatially densely sampled receiver gathers of the MCS shots.

Data processing consisted of the following two steps: (1) determination of sensor orientation and waveform rotation of horizontal components into radial (parallel to shooting direction) and transverse (orthogonal to shooting direction) directions (Anderson et al., 1987; Duennebier et al., 1987). To estimate the rotation angle, we use P_{water} arrivals for traces up to 17-km offset. The polarization angle of each trace was determined by linear least squares fitting the particle motion of the two horizontal components. The rotation angle is the median average of all traces within ±17-km offset. (2) Bandpass filtering (3–5–20–25 Hz) and predictive deconvolution (operator length of 300 ms, prewhitening of 0.1%, and prediction lags of 100 and 50 ms for the vertical and horizontal components, respectively) (Figures 2b and 2c). Analysis of the P_iS modes

Table 1
Sites information

Site	Line	Latitude	Longitude	Water depth (m)	Basement depth (m)	Sediment thickness (twtt s)	ΔT (s)	γ_{avg}	Error
1	3	44.2623	−125.3291	2,958	5,762	2.242	2.04	2.82	±0.09
2	3	44.3933	−125.3709	2,946	5,892	2.290	2.14	2.87	±0.09
3	3	44.5398	−125.4154	2,908	5,774	2.279	2.21	2.94	±0.09
4	1, 3	44.6547	−125.4506	2,859	5,645	2.302	2.14	2.86	±0.09
						2.280	2.19	2.99	±0.09
5	3	44.7996	−125.4968	2,816	5,507	2.167	2.07	2.91	±0.09
6	3	44.9197	−125.5327	2,772	5,432	2.055	1.94	2.89	±0.10
7	3	45.0867	−125.5816	2,719	5,732	2.351	2.19	2.86	±0.08
8	3	45.2356	−125.6316	2,656	5,271	2.001	1.79	2.79	±0.10
9	3	45.3815	−125.6775	2,596	5,229	2.104	2.00	2.90	±0.10
10	3	45.5275	−125.7231	2,458	5,130	2.210	2.02	2.83	±0.09
11	3	45.6571	−125.7697	2,392	5,139	2.193	2.12	2.93	±0.09
12	3	45.8351	−125.8185	2,315	4,999	2.137	2.07	2.94	±0.09
13	3	45.9674	−125.8605	2,432	4,875	1.955	1.85	2.89	±0.10
14	3	46.1117	−125.9095	2,597	4,815	1.813	1.89	3.08	±0.11
15	3	46.2672	−125.9586	2,555	4,965	1.973	2.13	3.16	±0.10
16	3	46.4012	−126.0036	2,572	4,567	1.748	2.03	3.32	±0.11
17	3	46.5448	−126.0515	2,643	4,637	1.705	2.00	3.35	±0.12
18	3	46.6890	−126.0987	2,614	4,736	1.794	2.09	3.33	±0.11
19	3	46.8354	−126.1487	2,595	4,934	1.931	2.11	3.19	±0.10
20	3	46.9814	−126.1970	2,574	5,016	1.993	2.12	3.13	±0.10
21	3	47.1275	−126.2457	2,524	5,034	1.904	1.88	2.98	±0.11
22	3	47.2719	−126.2931	2,479	5,262	2.094	2.13	3.03	±0.10
23	2, 3	47.4178	−126.3426	2,394	5,089	2.121	2.19	3.06,	±0.09
						2.100	2.14	3.04	±0.10
24	3	47.5503	−126.3858	2,333	5,144	2.200	2.25	3.05	±0.09
25	3	47.6826	−126.4284	2,281	5,115	2.191	2.13	2.94	±0.09
37	2	47.4635	−126.5544	2,383	4,476	1.848	2.11	3.28	±0.11
38	2	47.5032	−126.7436	2,438	4,209	1.622	1.94	3.39	±0.12
39	2	47.5434	−126.9346	2,505	3,971	1.645	1.68	3.04	±0.12
40	2	47.5835	−127.1271	2,528	3,624	1.100	1.74	4.16	±0.18
41	2	47.6227	−127.3193	2,581	3,551	0.949	1.44	4.03	±0.21
42	2	47.6626	−127.5170	2,617	3,022	0.375	0.86	5.59	±0.51
43	2	47.6989	−127.6925	2,642	3,242	0.499	0.93	4.73	±0.40
44	2	47.7389	−127.8978	2,622	3,013	0.381	0.98	6.15	±0.51
45	2	47.7756	−128.0849	2,638	2,994	0.337	0.84	5.99	±0.54
47	2	47.8496	−128.4719	2,651	2,988	0.323	0.82	6.08	±0.63
58	1	44.7281	−125.6840	2,846	4,820	1.809	1.99	3.20	±0.11
59	1	44.7777	−125.8545	2,877	4,390	1.475	1.70	3.31	±0.14
60	1	44.8274	−126.0266	2,832	4,244	1.385	1.69	3.44	±0.14
61	1	44.8795	−126.2003	2,806	4,107	1.277	1.60	3.51	±0.16
62	1	44.9298	−126.3774	2,804	3,861	0.998	1.44	3.89	±0.20
63	1	44.9797	−126.5484	2,828	3,712	0.897	1.37	4.06	±0.22
64	1	45.0275	−126.7200	2,847	3,648	0.828	1.33	4.21	±0.24
65	1	45.0795	−126.8947	2,843	3,550	0.721	1.22	4.39	±0.28
66	1	45.1404	−127.1135	2,867	3,298	0.454	0.90	4.97	±0.44
67	1	45.2018	−127.3304	2,876	3,535	0.679	1.18	4.48	±0.30
68	1	45.2508	−127.5089	2,887	3,388	0.507	1.13	5.46	±0.40
69	1	45.2999	−127.6869	2,861	3,301	0.479	1.00	5.18	±0.42
70	1	45.3494	−127.8662	2,928	3,638	0.714	1.11	4.11	±0.28
71	1	45.3971	−128.0455	2,843	3,581	0.768	1.39	4.62	±0.26
72	1	45.4463	−128.2230	2,813	3,032	0.204	0.87	9.53	±1.01
73	1	45.4938	−128.4029	2,802	2,908	0.117	0.62	11.64	±1.87
74	1	45.5402	−128.5789	2,781	3,013	0.229	0.79	7.90	±0.89
75	1	45.5876	−128.7598	2,775	2,925	0.151	0.71	10.43	±1.40
76	1	45.6350	−128.9408	2,778	2,856	0.084	0.52	13.42	±2.78
77	1	45.6814	−129.1182	2,740	2,762	0.058	0.26	9.89	±4.50
78	1	45.7271	−129.2992	2,715	2,863	0.164	0.65	8.94	±1.28

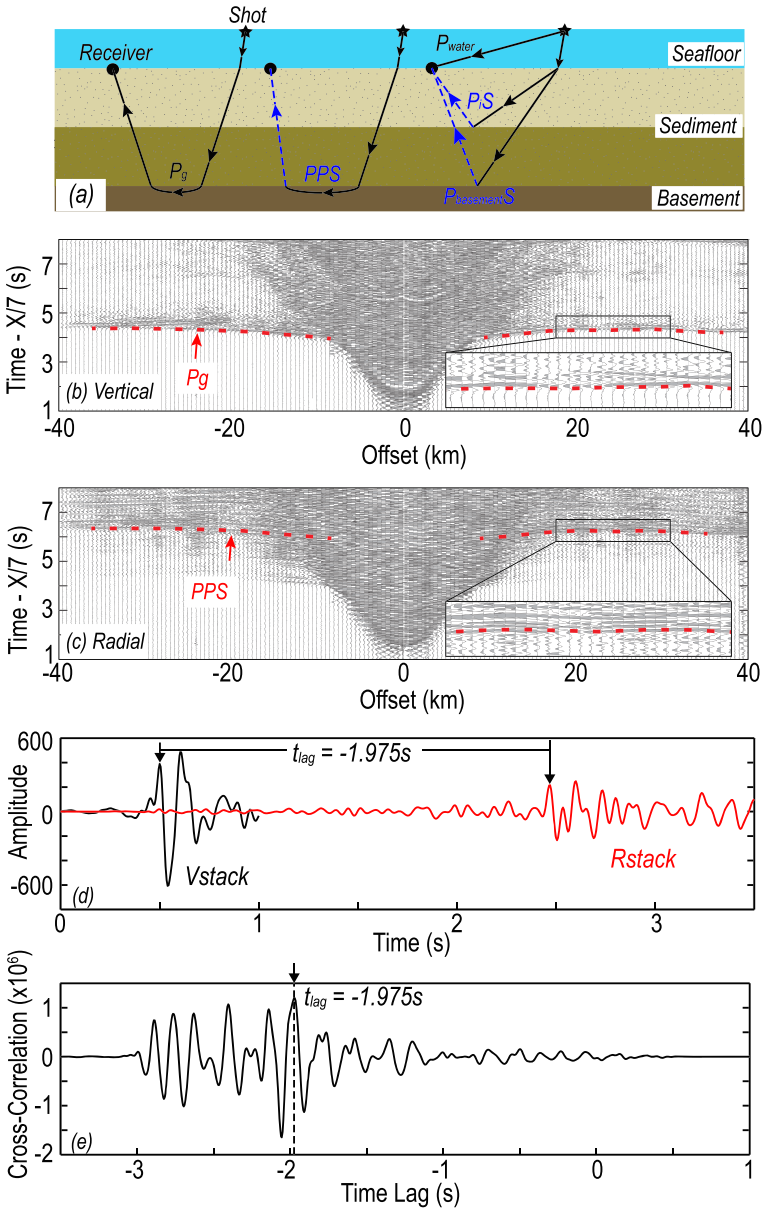

Figure 2. (a) Diagram of *P*, *PPS*, and *PiS* modes used in this study. Solid and dashed segments represent *P* and *S* waves, respectively. Processed data for OBS 06: (b) vertical and (c) radial components. Vertical axis is reduced travel time. Red curve in (b) and (c) indicates the P_g and *PPS* arrivals, respectively. (d) Time series of stacked vertical (*Vstack*, black) and radial (*Rstack*, red) waveforms located within 15- to 25-km offset. (e) Cross correlation of the *Vstack* and *Rstack*. The time lag between the P_g and *PPS* arrivals (between two arrows in (d)) corresponds to the maximum cross correlation at $t = -1.975$ s (vertical dashed line).

included an additional processing step for the receiver gathers of the MCS shots consisting of downward continuation of the radial component, simulating a different acquisition geometry in which source positions are near the seafloor (Arnulf et al., 2011; Harding et al., 2007). This process removes static time delays introduced by propagation through the water layer in the presence of variable seafloor depth and simplifies analysis of the nonhyperbolic normal moveout of P_iS modes (Tessmer & Behle, 1988). We downward continued traces within ±20-km offset, using a constant-velocity Kirchhoff integral formulation (Arnulf et al., 2014, 2018; Berryhill, 1984).

4. Methods and Results

4.1. Average *Vp*/*Vs* Ratio in Cascadia Basin Sediments

The average Vp/Vs ratio γ_{avg} of the sediment column beneath each OBS site can be expressed as follows (Tsuji et al., 2011):

$$\gamma_{avg}=\lfloor 2\Delta T+(T_{base}-T_{tsfl})\rfloor/(T_{base}-T_{tsfl}). \quad (1)$$

Here, $(T_{base}-T_{tsfl})$ is seafloor-to-basement two-way travel time beneath the OBS determined from coincident MCS reflection profiles (Han et al., 2016; Han et al., 2018), and ΔT is the time lag between the *Pg* and *PPS* arrivals. To determine ΔT for each OBS we first stacked waveforms for traces with 15- to 25-km offset for the vertical and radial components (*Vstack* and *Rstack*, respectively), thus increasing the signal-to-noise ratio. We then cross correlated a 1-s-long window of *Vstack* centered at the P_g arrival, with a 3.5-s-long window of *Rstack* containing the *PPS* arrival (Figure 2d), and the absolute value of the lag with maximum correlation coefficient is ΔT (Figure 2e). The estimated γ_{avg} uncertainty is calculated by taking into account the uncertainty of ΔT ($\pm$0.1 s) and of $(T_{base}-T_{tsfl})$ ($\pm$0.01 s). Results of γ_{avg} and their uncertainties are listed in Table 1. Figures 3a–3c show the spatial variation of γ_{avg} along the three profiles. Along Lines 1 and 2, γ_{avg} decreases approaching the CDF as sediments thicken (black solid curves in Figures 3a–3c).

Variation of γ_{avg} with respect to total sediment thickness for all sites is shown in Figure 3d. Results show a well-defined trend of decreasing γ_{avg} with depth, dropping sharply within the top 0.5 km of sediment. This trend indicates sediment compaction with depth (Dutta et al., 2009). The relationship between the γ_{avg} and sediment thickness z (km) can be best described with an exponential function (Figure 3d):

$$\gamma_{avg}=19.36\ e^{-2.96z}+3.03. \quad (2)$$

To assess the validity of this equation we compare the γ_{avg} predicted by our empirical function for $z=1$ km (3.57, black triangle in Figure 3d) with the reported value of $\gamma_{avg}=3.67$ in a location to the north of our study area where sediment thickness is 1 km (Au & Clowes, 1984), showing excellent agreement.

4.2. Intrasediment Interval *Vp*/*Vs* Ratio From Semblance Velocity Analysis of *P*-*S* Reflections

Our analysis of *PPS* modes has allowed us to estimate the average Vp/Vs of the full sediment column beneath each OBS but does not provide constraints on how the Vp/Vs structure varies with depth at each site. To obtain insights into the intrasediment Vp/Vs structure we take advantage of the P_iS modes, which are observed with very high signal-to-noise ratio in the near-offset traces of the MCS-shot radial record sections (Figures 4a, 4b, 5a, and 5b). The most prominent P_iS mode is $P_{Basement}S$, the *S*-converted reflection from the top of basement (Figures 4a, 4b, 5a, and 5b). Between this arrival and the direct water wave we observe several other arrivals that correspond to *S*-converted reflections from intrasediment interfaces.

We do not attempt to model directly the travel times of the P_iS arrivals using a forward ray-tracing approach (e.g., Peacock et al., 2010). This is because, although high-quality coincident MCS images of the sedimentary sequence exist (Han et al., 2016, 2018), correlating a particular P_iS arrival with a particular MCS reflector is not straightforward (except for basement) as it would require an a priori guess of the Vp/Vs structure to convert MCS *P* two-way travel times to *PS* times, which may bias results. Also, the sparseness of the OBS distribution (15 km apart from each other) prevents us from exploring the Vp/Vs structure in a 2-D manner, either by forward modeling or by tomographic inversion of P_iS travel times. For these reasons we model the intrasediment Vp/Vs structure in 1-D as a function of depth for each OBS independently. We perform nonhyperbolic normal moveout semblance velocity analysis (Yilmaz, 2001) of the downward continued gathers (Figures 4b and 5b). We chose the downward continued over the original gathers because in the former, travel time variations due to seafloor topography have been eliminated and because eliminating the down propagation through the water column facilitates the application of the nonhyperbolic normal moveout equations for *S*-converted waves, which are derived assuming both down-going and up-going asymmetric ray paths through a stratified medium (Tessmer & Behle, 1988; Yilmaz, 2001).

The semblance velocity analysis of P_iS modes requires a priori definition of a root-mean-square (RMS) *P* wave velocity (Vp^{RMS}), which we obtain from published *Vp* models in our study area (Canales et al., 2017;

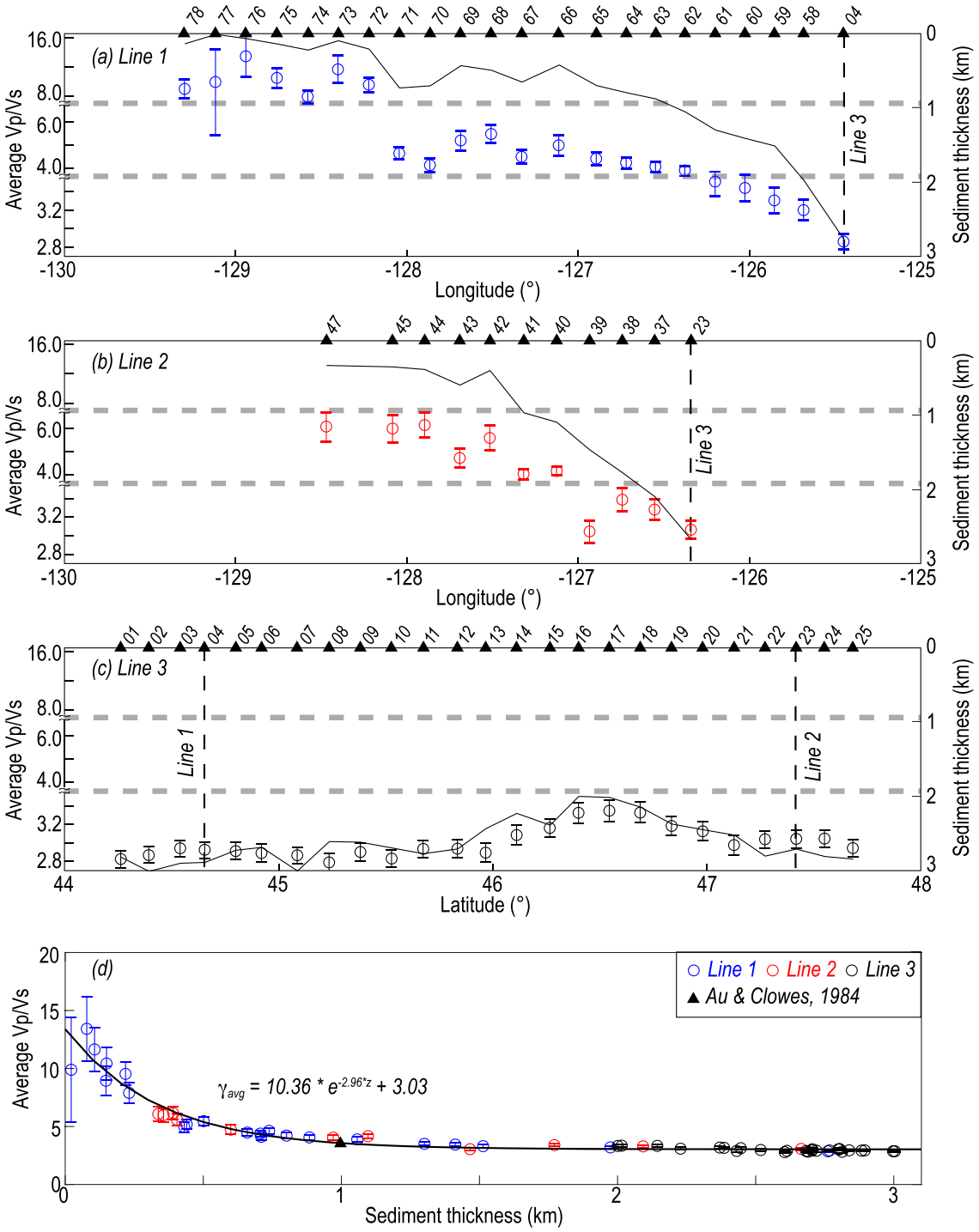

Figure 3. Spatial variation of average *Vp*/*Vs* (open circles with error bars) and sediment thickness (black solid line) along (a) Line 1, (b) Line 2, and (c) Line 3. Black triangles represent the OBS sites. Horizontal dashed gray lines indicate changes in *Vp*/*Vs* vertical scale for clarity purposes. (d) Variation of γ_{avg} with respect to seafloor-to-basement depth (i.e., converting interface). Blue, red, and black circles represent results from Lines 1, 2, and 3, respectively. Black solid curve is the best fitting exponential function. Black triangle shows γ_{avg} estimated on the Juan de Fuca plate at a site north of our study area over a 1-km-deep basement (Au & Clowes, 1984).

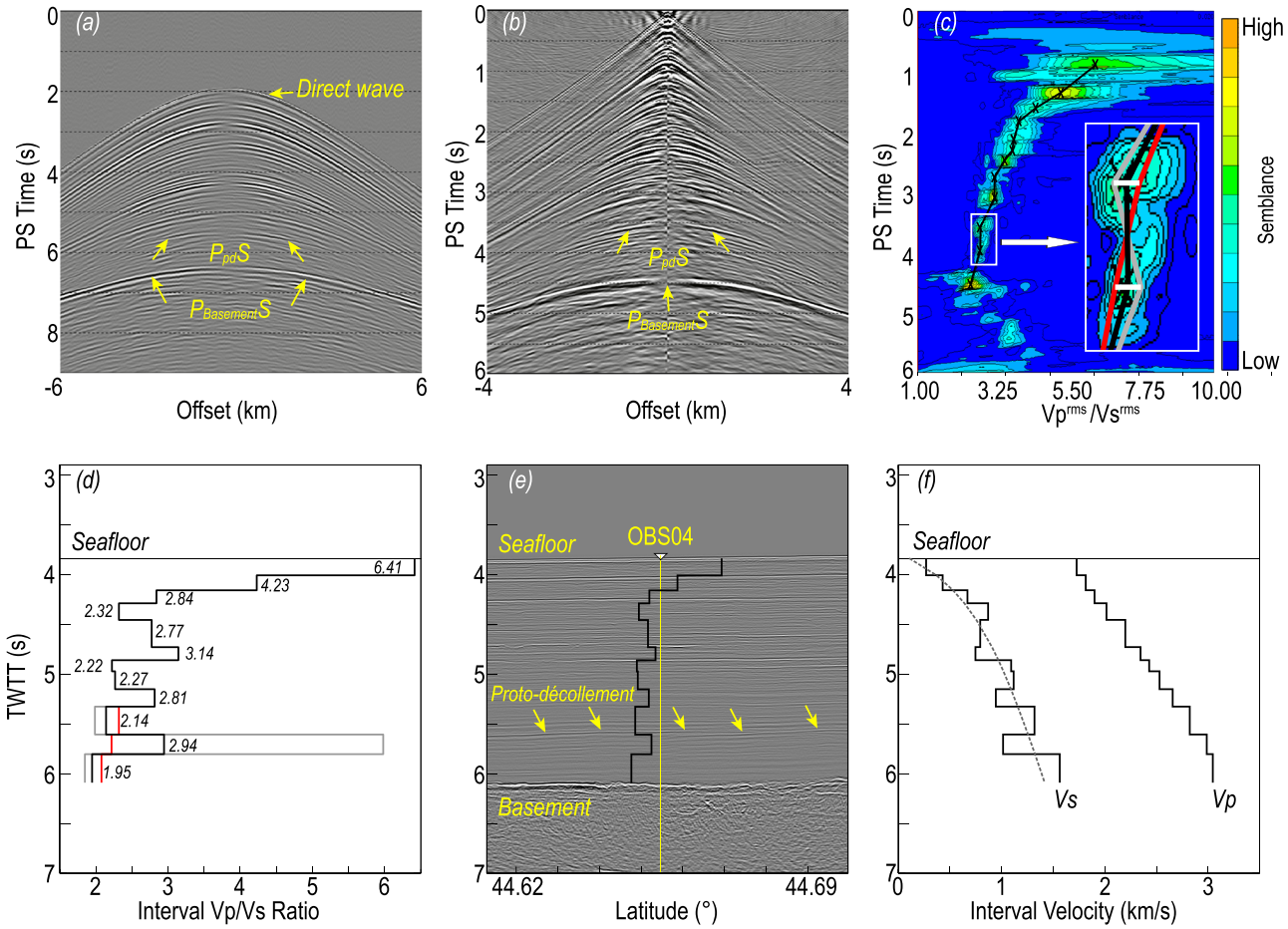

Figure 4. Example of calculating intrasediment *Vp*/*Vs* for OBS 04. (a) Radial component record section of MCS shots. Yellow arrows show direct wave, *PS* reflection from the basement ($P_{\text{Basement}}S$) and from the proto-décollement ($P_{\text{Pd}}S$). (b) The same data as (a) after downward continuation of sources to the seafloor. (c) Contoured semblance velocity spectrum of downward-continued gather shown in (b) in time (t^{PS}) – gamma ($\gamma^{RMS} = Vp^{RMS}/Vs^{RMS}$) domain. Black crosses connected with solid line indicate picked *PS* arrivals with high semblance. Inset is a zoomed-in window of the smaller white box left of the white arrow to illustrate the sensitivity of results to user picking errors. Horizontal white bars correspond to ±3% of the semblance picks bounding the layer immediately beneath the proto-décollement. Red line shows a hypothetical $t^{PS} - \gamma^{RMS}$ function in which semblance picks for the top and bottom of this layer are overpicked and underpicked by 3%, respectively. Gray line corresponds to the opposite scenario in which top and bottom semblance picks are underpicked and overpicked by 3%, respectively. (d) Calculated interval *Vp*/*Vs* ratio (γ) beneath OBS 04 as a function of *P* wave two-way travel time (black, with interval *Vp*/*Vs* values labeled). Red and gray lines correspond to the same-color hypothetical $t^{PS} - \gamma^{RMS}$ functions in (c). (e) MCS section of Line 3 in the vicinity of OBS 04 (from Han et al., 2018) showing sediment layering and oceanic basement and calculated γ function from (d) shown for comparison (black). (f) Interval *Vp* and *Vs* functions from this study as a function of two-way travel time (solid black) compared to *Vs* calculated according to Bell et al. (2015) (dashed gray).

Han et al., 2017; Horning et al., 2016), and consists of a semblance velocity spectrum in which a user can pick γ^{RMS}-*PS* time pairs corresponding to coherent arrivals with high semblance (Figures 4c and 5c). Here γ^{RMS} corresponds to the ratio between RMS *Vp* and *Vs* functions (Vp^{RMS}/Vs^{RMS}). About 6–14 *PS*-conversion interfaces are identified below each site. Contoured semblance peaks thus indicate a strong *PS* conversion at the time t^{PS} with corresponding γ^{RMS}. Output (t^{PS}, γ^{RMS}) pairs are then converted to two-way *P* wave travel time (t^{PP}) and interval *Vp*/*Vs* ratio, γ using the Dix equation (Yilmaz, 2001) (Figures 4d and 5d).

Calculated interval γ as a function of t^{PP} for Sites OBS 04 and 23 is shown in Figures 4d and 5d (black curve), respectively. At OBS 04 (Figure 4d), γ is high (6.41) in the shallowmost sediment and gradually decreases to 1.95 at the basement. However, the general decrease of γ with depth shows significant variability, with layers of both elevated and reduced *Vp*/*Vs*. Comparing the interval *Vp*/*Vs* functions with the coincident MCS images shows that, in many cases, there is a good correlation between discontinuities that produce detectable P_iS waves (i.e., jumps in the interval *Vp*/*Vs* functions) and MCS reflectors. For example, beneath OBS

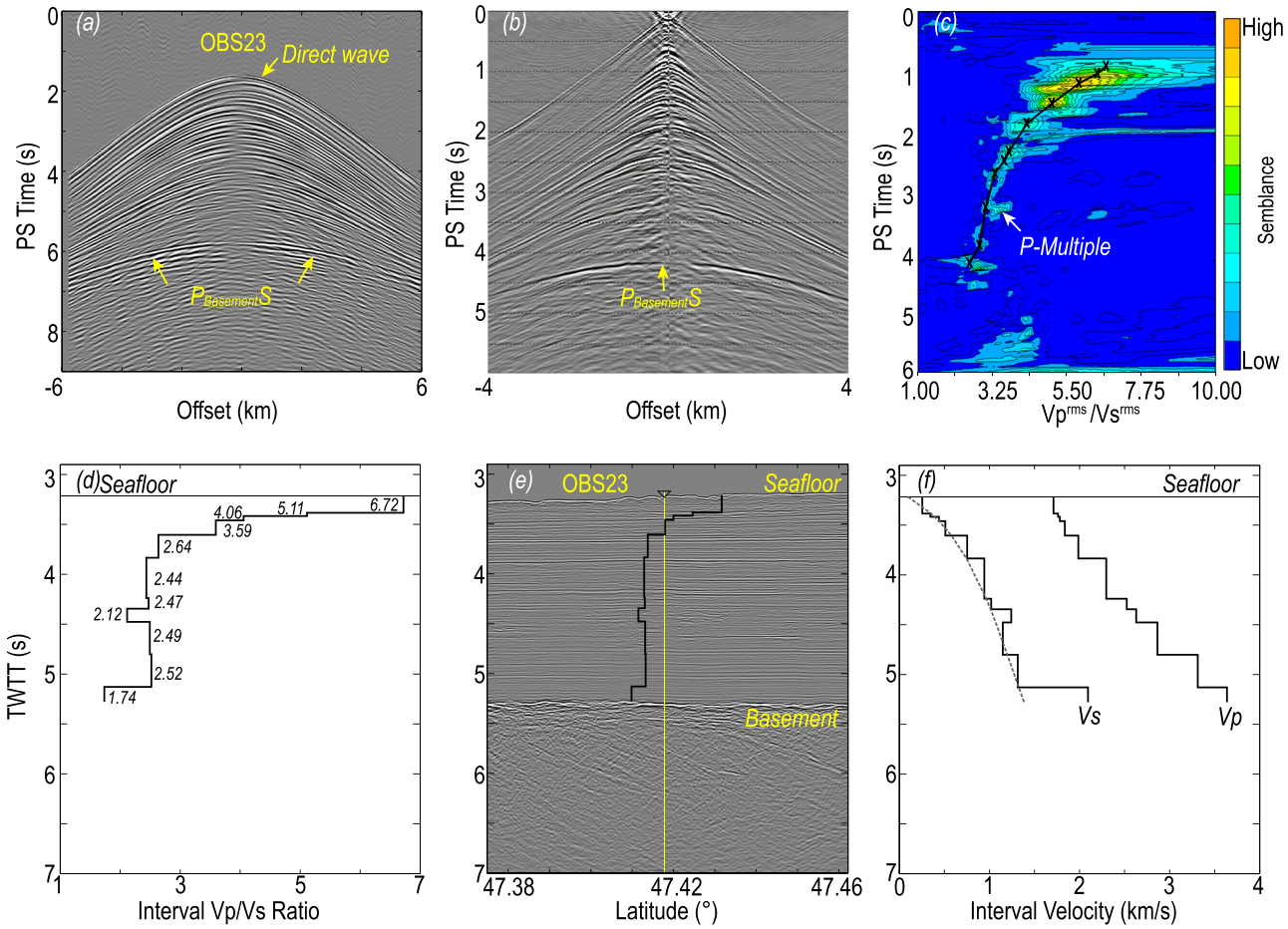

Figure 5. The same as Figure 4 for OBS 23. White arrow in (c) shows high semblance associated to arrivals from a primary water multiple that could be misinterpreted as a P_iS conversion.

04 prominent shallow reflectors at ~4.0 and ~4.2 s correlate with large decreases in γ (Figure 4e). Deeper in the sediments, a layer with relatively elevated γ (3.14 at ~4.8 s) is bounded at the top by a short strong reflector and at the bottom by a strong, laterally continuous reflector, and layers with $\gamma = 2.81$ and 2.94 at ~5.2 and ~5.8 s, respectively, are both limited at the top by laterally continuous reflectors. In the case of the layer with $\gamma = 2.94$, it is bounded at its top by a reversed-polarity reflector where the proto-thrusts shoal (Cochrane et al., 1994; Han et al., 2016, 2017). The correlation between our interval *Vp*/*Vs* functions and the coincident reflectivity images is not always as good as that found for OBS 04 (Figure 4e), which may be due to inaccuracies in the *Vp* models that prevent an accurate mapping of events from the t^{PS} to the t^{PP} domain. At OBS 23 (Figure 5d), γ also shows a gradual decrease with depth from 6.72 in the shallowmost sediment to 1.74 at the basement. Compared to the structure beneath OBS 04, the *Vp*/*Vs* structure beneath OBS 23 is much smoother.

To gain a sense of the sensitivity of the calculated interval *Vp*/*Vs* values to potential user picking inconsistencies during the semblance velocity analysis, we present two extreme cases over estimating and underestimating the interval *Vp*/*Vs* within a particular layer. For these tests we chose the layer beneath the reversed-polarity reflector at the location of OBS 04 discussed above. We test overpicking and underpicking of semblance picks by ±3% of the preferred values. The choice for the magnitude of this deviation is somewhat arbitrary, but it captures well the width of high semblance regions in the semblance velocity spectrum maps. Interval *Vp*/*Vs* within the layer could be underestimated if the user overpicked and underpicked the semblance picks corresponding to the top and bottom of the layer, respectively (red line in Figures 4c inset and 4d). In this case, an interval *Vp*/*Vs* value of 2.2 in this layer would result in progressively decreasing

values in the deepest sediments, instead of the elevated value of 2.94 in our preferred solution. This is because the overestimation and underestimation of the top and bottom semblance picks smoothen out the general trend of the RMS *Vp*/*Vs* function at that depth. Conversely, interval *Vp*/*Vs* within the layer could be grossly overestimated if the user underpicked and overpicked the top and bottom semblance picks, respectively (gray line in Figures 4c inset and 4d). In this case, underestimation and overestimation of the top and bottom semblance picks magnify the subtle inversion in RMS *Vp*/*Vs* function at that depth, yielding an unrealistic interval *Vp*/*Vs* of 6.0. These tests show that results are very sensitive to the uncertainties in picking of the semblance maps. For this reason we restricted picking to only well-defined high semblance points surrounded by closed contours. Also, the variability obtained in the sensitivity tests does not represent the true uncertainty of our results because all picks were done in a consistent manner across the data set. Thus, any inherent errors would be similar across the whole data set, making comparison between sites meaningful and results robust.

To gain additional confidence in our results, we compare interval *Vs* functions derived from the interval *Vp* and *Vp*/*Vs* functions with the general *Vs* profile for Cascadia Basin sediments obtained from analysis of Rayleigh waves recorded in the Cascadia Initiative passive OBS array (Bell et al., 2015). Figures 4f and 5f show the interval *Vs* calculated in this study for OBSs 04 and 23, respectively, compared to *Vs* from Bell et al. (2015), illustrating excellent agreement between the two models.

The approach described above was applied to 23 OBS sites along Line 3 and four additional sites along Lines 1 and 2 that are closest to the CDF (Figure 1). Figure 6 shows the results of calculated interval γ on top of the coincident MCS images. The most striking pattern that emerges when comparing all of the interval γ functions is that all 13 sites located to the south of 46°N (i.e., OBS 2–13, 58, and 59) show large variability at depth (Figure 7b), while interval γ functions to the north of 46°N are more similar to each other, characterized by well-defined compaction trends with a relatively monotonous decrease of *Vp*/*Vs* with depth (Figure 7a). To demonstrate this difference north and south of 46°N, we somewhat arbitrarily define the interval γ of a particular layer as "elevated" or "reduced" if it is 10% higher or lower, respectively, than that of the layers above and below (e.g., red or cyan arrows in Figure 6). All 13 southern sites have sediment layers associated with both elevated and reduced γ, while only 8 of a total of 14 northern sites have sediment layers associated with elevated or reduced γ (Figures 6, 7a, and 7b).

5. Interpretations and Discussion

Our results show along-strike variations in the properties of sediments seaward from the CDF, with sediments off central Oregon (Figure 7b) showing evidence for pronounced *Vp*/*Vs* contrasts, in comparison to smoother *Vp*/*Vs* profiles off northern Oregon and Washington (Figure 7a). A number of factors may influence *Vp*/*Vs* in sediments, including pore pressure, porosity, clay content, and stress-induced or inherent anisotropy (e.g., Blangy et al., 1993; Han et al., 1986; Zimmer et al., 2002). Some of these properties such as *Vp* and porosity of incoming sediments vary as a function of distance to the deformation front due to consolidation and fluid expulsion (Cochrane et al., 1994; Han et al., 2017; Yuan et al., 1994), and stresses in the proto-thrust zone seaward from the deformation front are likely to affect sediment properties. Therefore, it is plausible that variable distance of our OBS locations to the CDF could be a factor contributing to the along-strike variability we find in *Vp*/*Vs* structure. However, we do not find that the regional along-strike variations in *Vp*/*Vs* structure correlate with distance from the OBS sites to the deformation front. The southernmost Sites 02–04 are located ~8–10 km from the CDF and display heterogeneous *Vp*/*Vs* functions, while northernmost Sites 22–25 located at similar distances from the CDF are characterized by homogeneous *Vp*/*Vs* functions.

We therefore focus our interpretations and discussion on the possible influence of mineralogy, effective stress, and excess pore pressures to explain the estimated *Vp*/*Vs* values and their variability. In the following sections we first derive a *Vp*/*Vs* compaction curve from our results and interpret it in terms of the dominant compositions of the sediments. We then derive a porosity compaction curve from a compilation of the IODP porosity measurements in the Cascadia Basin and use it to interpret our *Vp*/*Vs* results in terms of effective stress and pore pressure following the approach of Skarbek and Saffer (2009). Finally, we discuss the role of variations in clay content and clay mineralogy, excess pore pressures related to the development of the proto-décollement, and their implications for sediment deformation at Cascadia accretionary prism.

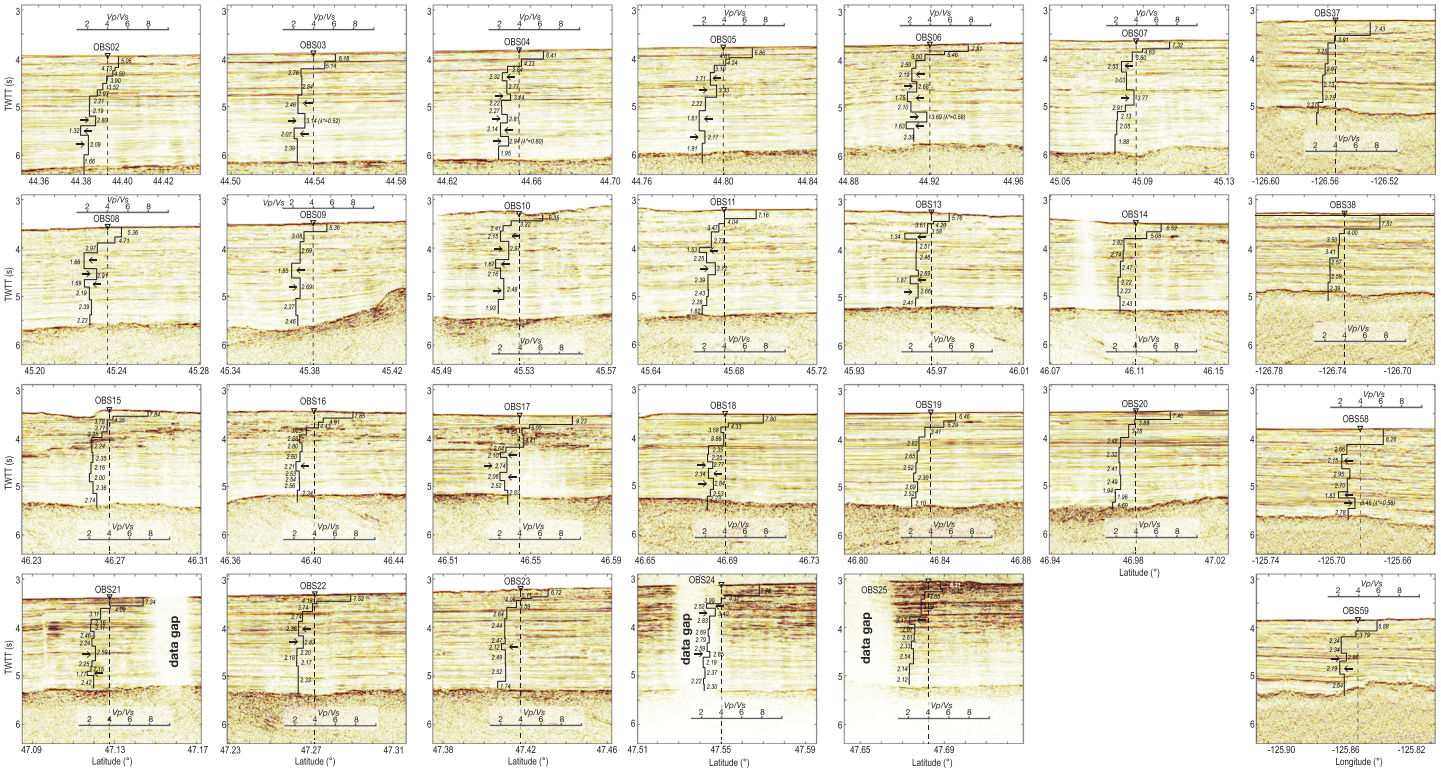

Figure 6. Calculated interval *Vp*/*Vs* functions for all 27 sites, all plotted at the same scale. Background is the MCS section in the vicinity of the corresponding site. Layers with *Vp*/*Vs* at least 10% higher or lower than adjacent layers are marked with right or left arrow, respectively.

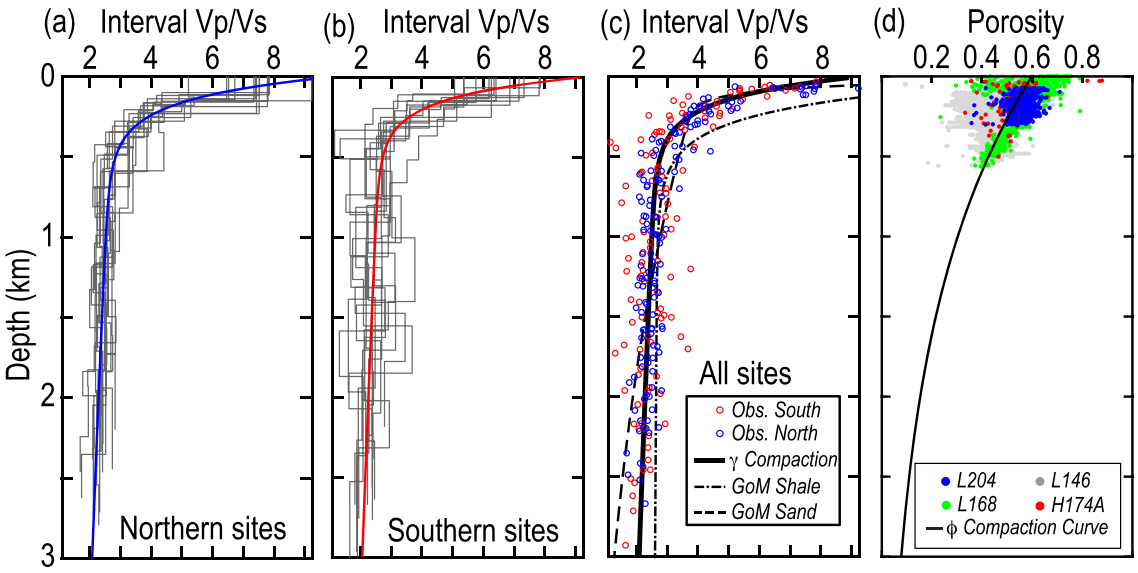

Figure 7. (a) Interval *Vp*/*Vs* functions as a function of depth for the northern sites. Blue curve is the *Vp*/*Vs* compaction curve derived from this subset of functions. (b) The same as (a) for the southern sites. Red curve is the *Vp*/*Vs* compaction curve derived from this subset of functions. (c) Interval *Vp*/*Vs* values for all sites (red and blue open circles for southern and northern sites, respectively). Solid line is the compaction curve derived from all sites. Dash-dotted and dashed lines are empirical compaction curves from Dutta et al. (2009) for shale and clean brine sand, respectively. (d) Porosity as a function of depth. Data were compiled from measurements in Cascadia sediment samples from ODP Leg 204 Sites 1,244–1,252 (Shipboard Scientific Party, 2003) (blue circles), ODP Leg 146 Sites 888–892 (Shipboard Scientific Party, 1994) (gray circles), ODP Leg 168 Sites 1,023–1,032 (Shipboard Scientific Party, 1997b) (green circles), and DSDP Leg 18 Site 174 (Shipboard Scientific Party, 1973) (red circles). Solid curve shows the best fitting trend derived from them using an exponential decrease with depth (Equation 4).

5.1. *Vp/Vs* and Porosity Compaction Curves and Effective Stress

We derived a *Vp*/*Vs* compaction curve for all analyzed sites (Figure 7c). Compaction curves derived separately for the northern and southern sites are essentially the same, with only minor differences in the upper 500 m (Figures 7a and 7b). Thus, despite the north-south variability in interval γ functions, the following compaction curve is adequate for all sites:

$$\gamma = 6.672\ e^{-7.299z} + 2.278\ e^{-0.09z}. \tag{3}$$

Drilling indicates that Cascadia Basin sediments include layers of hemipelagic muds and turbidites of variable clay, silt and sand contents, and grain sizes, with sands being more abundant in the upper few hundred meters and rarely present below (Shipboard Scientific Party, 1973, 1997a). Petrophysics and borehole analysis of sands and clay-dominated shales from the Gulf of Mexico show that *Vp*/*Vs* in sands and shales decreases with depth following distinct compaction curves (Dutta et al., 2009) (Figure 7c). Comparing with the sand and shale compaction curves of Dutta et al. (2009), our results suggest a sand-dominated composition in the upper ~400 m, transitioning to a clay-dominated composition at ~700-m depth (as indicated by the similar slopes of our compaction curve and the clay curve below this depth), consistent with drilling observations.

We derived a porosity compaction curve using a compilation of porosity (ϕ) and depth measurements in sediments from ODP and DSDP drilling legs (Figure 7d):

$$\phi = 0.6\ e^{-0.682z}, \tag{4}$$

where z is depth below seafloor in kilometer. This equation is comparable to that describing porosity versus depth for Cascadia sediments derived from RMS *Vp* measurements using MCS data by Yuan et al. (1994) $\phi = 0.6\ e^{-z/L}$, for values of $1.5 \leq L \leq 2.5$, which is based on velocity-porosity relationships from the Nankai Trough accretionary prism (Hyndman et al., 1993). We calculate effective stress (or differential pressure, P_d) from our *Vp*/*Vs* measurements following Skarbek and Saffer (2009).

$$P_d = \frac{\left(\rho_s - \rho_f\right)g}{b}\left[\left(1n\phi_0 - \phi_0\right) - \left(1n\phi - \phi\right)\right], \tag{5}$$

where ϕ is porosity, $\phi_0 = 0.6$ and $b = 0.682\ \mathrm{km}^{-1}$ are the porosity at the seafloor and the compaction constant, respectively (Equation 4), ρ_f is the fluid density (1,030 kg m^{-3}), ρs is the solid grain density (2,750 kg m^{-3}), and g is gravitational constant (9.8 m s^{-2}). If the porosity at the depths corresponding to our interval *Vp*/*Vs* estimates (Figure 7c) follows Equation 4, then we can convert the interval *Vp*/*Vs* estimates into porosity estimates using Equations 3 and 4 and subsequently estimate the effective stress associated to each of our interval *Vp*/*Vs* values using Equation 5 (Figure 8a).

5.2. Compositional Controls on *Vp/Vs*

5.2.1. Variations in Clay Content

The calculated effective stress results are shown in Figure 8a, compared against the *Pd*-*Vp*/*Vs* trends of Prasad (2002) for sand and of Huffman and Castagna (2001) for clean sands and sands containing 8-wt.% clay. Our results show the expected increase of *Vp*/*Vs* with decreasing effective stress (e.g., Lee, 2003) but with significant scatter. Comparison of the *Vp*/*Vs* values that we have flagged as anomalously elevated with those flagged as anomalously low (Figure 6) indicates that variations in clay content could potentially explain the observed scatter. For example, layers with high sand content embedded within sedimentary layers of higher clay content could lead to the anomalous, more variable *Vp*/*Vs* structures that we find at the southern sites. At the northern sites, less prevalent presence of sandy layers could lead to the more homogeneous interval *Vp*/*Vs* functions we observe.

Greater abundance of sandy layers in the southern sites could be favored by the characteristics of sediment transport in this region because more energetic, larger grain size particles (i.e., sands) can be transported downslope from the continental shelf to the abyssal plain to greater distances from their sources than smaller particles. Sediment transport at the Cascadia margin is dominated by supply of sediment from the Fraser River through the Juan de Fuca Straight and the Columbia River and transport along a southward

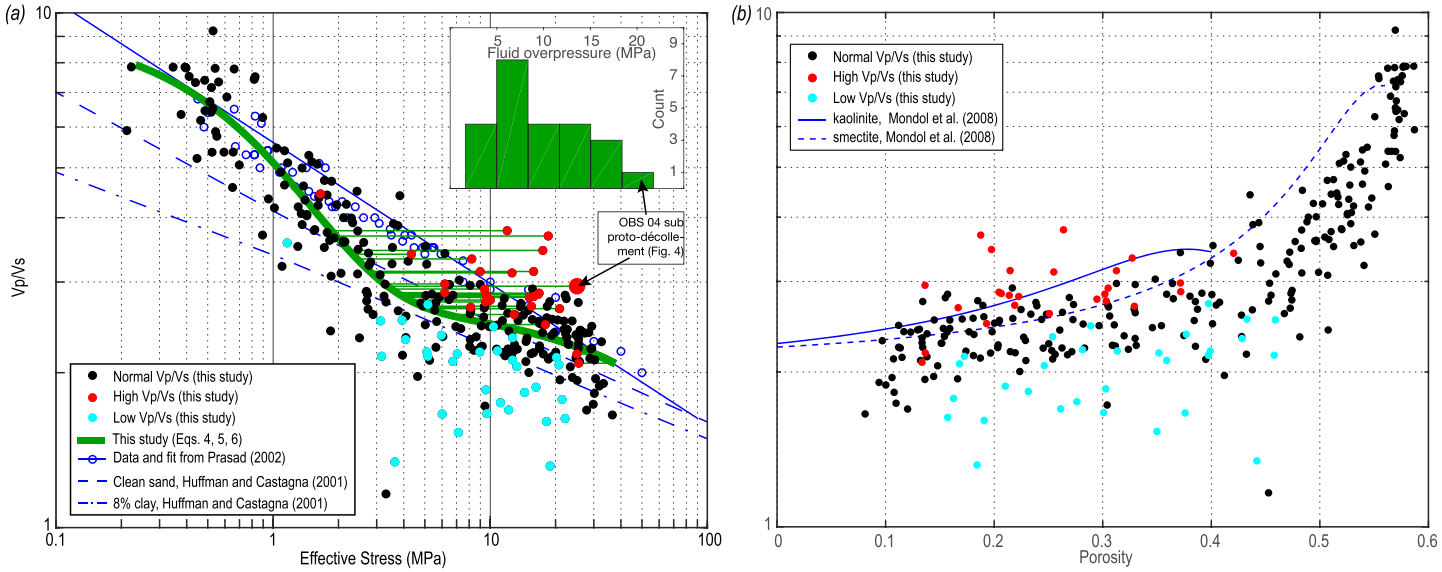

Figure 8. (a) Interval *Vp*/*Vs* as a function of effective stress in log-log space. All solid circles are from this study: red and cyan for elevated and reduced *Vp*/*Vs*, respectively, and black for all others. Larger solid red circle corresponds to the *Pd*-*γ* pair of the sub-proto-décollement layer at the location of OBS 04. Blue open circles are data from Prasad (2002), and blue solid curve is the linear trend of these data. The blue dashed and dotted dashed lines are linear trends from measurements in sediment samples of clean sand and 8% clay, respectively, from Huffman and Castagna (2001). This green line shows the trend expected from combining Equations 3, 4, and 5. Horizontal green bars illustrate the fluid overpressures required to decrease the effective stress of the layers with elevated *Vp*/*Vs* values if these were due to anomalously elevated porosities. Inset shows a histogram of these fluid overpressures. (b) *Vp*/*Vs* ratio as a function of porosity in log-linear space for kaolinite (solid) and smectite (dashed) determined from Equations A1 and A2 (Mondol et al., 2008). All solid circles are from this study: red and cyan for elevated and reduced *Vp*/*Vs*, respectively, and black for all others.

anastomosing network of canyons and deep-sea channels that coalesce into the Cascadia Channel and across the Blanco transform (e.g., Griggs & Kulm, 1970; Underwood et al., 2005). Therefore, the predominantly southward pattern of sediment transport from the western North American margin to Cascadia Basin could potentially favor a southward increase in the relative content of sandy layers, leading to the variability in *Vp*/*Vs* structure we observe (Figures 6 and 7). However, we would expect that this mechanism leads to more laterally continuous layers of anomalous *Vp*/*Vs*, contrary to our observations that show a more heterogeneous structure at lateral scales of our OBS spacing (~15 km).

5.2.2. Variations in Clay Mineralogies

At the Cascadia margin there are documented geographical trends in the relative abundances of clay minerals in accreted as well as in abyssal plain near-surface sediments thought to result from sediment dispersal by turbidity and seasonal oceanographic currents, as well as changes in glacial-interglacial weathering products (Karlin, 1980; Underwood, 2002; Underwood & Hoke, 2000). Smectite content of the clay-sized fraction exceeds 50% near the mouth of the Columbia River and decreases southward along the continental slope and into the abyssal plain to values of 20% and less (Karlin, 1980; Underwood, 2002). Such changes extend into the abyssal-plain hemipelagic section overlying igneous basement in Cascadia Basin sediments (Underwood, 2002). Chlorite content shows the opposite trend, with the highest values (>50%) found offshore southern and central Oregon, while illite content is relatively constant with the exception of southern Oregon where it is higher (Karlin, 1980). Therefore, regional variations in the relative abundances of clay minerals could potentially play a role in the presence of layers with anomalous *Vp*/*Vs* at the southern sites.

The *Vp*/*Vs* ratio of clay minerals is not well constrained due to their fine-grained nature, and there is little agreement among existing measurements (e.g., Katahara, 1996; Mondol et al., 2008; Vanorio et al., 2003; Wang et al., 2001). Here we consider the empirical relationships of Mondol et al. (2008) relating elastic constants and porosity derived from laboratory measurements in brine-saturated aggregates of two end-member clay minerals: fine-grained smectite and coarse-grain kaolinite (Appendix A). We find that for the range of porosities expected at the depths of the layers with anomalous *Vp*/*Vs* values at the southern sites

(approximately <40%, Figure 7d), kaolinite has higher *Vp*/*Vs* than smectite (Figure 8b). Although the difference in *Vp*/*Vs* between kaolinite and smectite for a given porosity is smaller than the scatter of our observations, it is not negligible (Figure 8b). Therefore, the lower relative abundance of smectite and higher abundance of other coarser-grained clay minerals off central Oregon (Karlin, 1980; Underwood, 2002) could be an important factor contributing to the presence of layers with elevated *Vp*/*Vs* at the southern sites in our study. However, for the same reasons discussed for the clay content hypothesis in the previous section, regional variations in clay mineralogy should result in more laterally continuous layers of anomalous *Vp*/*Vs*, contrary to our observations of heterogeneous structure.

5.3. Fluid Overpressure

An alternative explanation for the anomalously elevated *Vp*/*Vs* values and variability of *Vp*/*Vs* functions offshore central Oregon is the presence of layers with fluid overpressures associated with anomalously high porosities at depth (e.g., Prasad, 2002; Zimmer et al., 2002). Elevated pore pressure lowers the effective stress, thus reducing the shear strength of sediments (e.g., Huffman & Castagna, 2001). Equations 3 to 5 can be combined to derive an empirical curve describing the trend of *Vp*/*Vs* as a function of effective stress for Cascadia Basin sediments (Figure 8a). Considering the anomalously elevated *Vp*/*Vs* values, departure from this trend of the *Pd*-γ pair estimates, under the assumption of normal porosities at depth, provides an upper limit of fluid overpressures associated with those anomalous *Vp*/*Vs* values (Figure 8a inset). We find that the anomalously elevated *Vp*/*Vs* values correspond to fluid overpressures ranging from 2 to 22 MPa (Figures 8a inset and 9a).

A more intuitive description of fluid overpressures is given by the excess pore pressure parameter or normalized pore pressure ratio, λ^*, defined as the ratio between fluid overpressure and the differential pressure between lithostatic and hydrostatic pressure (Shi & Wang, 1988; Tsuji et al., 2008). The normalized pore pressure ratio is 0 when pore pressure is hydrostatic and approaches 1 when pore pressure approaches the lithostatic overburden (Shi & Wang, 1988). For the layers with anomalously elevated γ (Figures 6 and 8a), our calculations result in λ^* ranging between 0.2 and 0.6 (Figure 9b).

We find that layers with the highest λ^* values (>0.5) are found beneath OBS Sites 03, 04, 06, and 58 (Figure 6), which are all located to the south of 45°N, and all these layers are found within the lower half of the incoming sediment section (Figures 9b and 9c). This finding is consistent with results of Han et al. (2017) that show reduced *Vp* in deep sediments south of 44°48′N compared to higher *Vp* in sediments to the north, which was interpreted by these authors as evidence for underconsolidation of deep incoming and accreted basal sediments offshore central Oregon. This spatial correlation suggests that anomalously high *Vp*/*Vs* within some of the sedimentary layers is likely due to elevated pore pressure resulting from underconsolidation of deep sediments (Han et al., 2017), and we favor this interpretation over the compositional controls discussed in section 5.2. The layers with elevated *Vp*/*Vs* and pore pressure are likely to be bounded on the top by low-permeability sediments that inhibit fluid drainage from deeper sediments and the oceanic crust. The regional north-south variations we observe thus could be explained if there is a higher abundance of lower permeability clays relative to higher permeability sediments (e.g., silty clays, clayey silts, and sandy clays) (Bryant, 2003) in the intermediate to deep sediments offshore central Oregon than offshore Washington.

5.4. Implications for Décollement Development and Accretionary Wedge Deformation

The layer with the highest predicted fluid overpressure (22 MPa) and λ^* (0.6) is located at OBS Site 04 (Figures 8a and 9) immediately beneath a reflector corresponding to the stratigraphic level at which the proto-thrusts shoal (Figure 4e). This negative polarity reflector has been referred to previously as a proto-décollement (Cochrane et al., 1994; Han et al., 2016). We follow this nomenclature for consistency with earlier studies, although it has been shown recently that, offshore central Oregon near the deformation front and in the frontal wedge, the décollement where the frontal major thrust faults shoal is located at a shallower level than this reflector (Han et al., 2017). That the layer with the highest estimated overpressure coincides with the proto-décollement strongly suggests that excess pore pressures capped by low-permeability layers control the depth at which the proto-thrust shoals.

As mentioned above, we find the highest λ^* values (>0.5) south of 45°N and within the lower half of the sediment column (Figures 9b and 9c), suggesting that proto-décollement development within the incoming

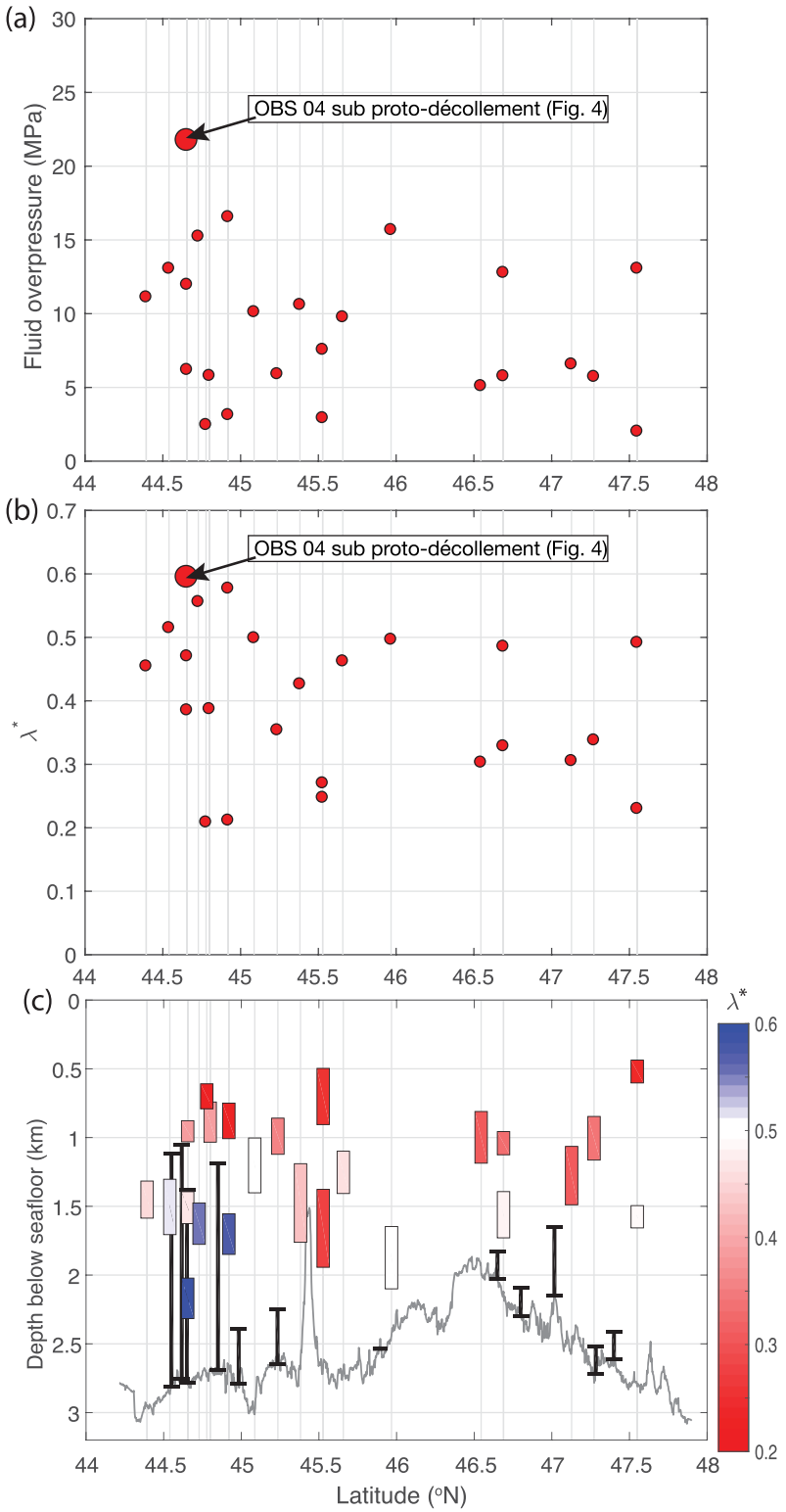

Figure 9. (a) Fluid overpressure as a function of OBS latitude for layers with elevated interval *Vp*/*Vs* (the same data as in Figure 8a inset). (b) The same data as in (a) converted to normalized pore pressure ratio λ^*. (c) The same data as in (b) shown as a function of both latitude and depth below seafloor (rectangles colored according to λ^*). Vertical extent of rectangles represents the thickness and depth of the layers with elevated interval *Vp*/*Vs*. Gray line shows sediment thickness along profile L3. Vertical black bars show the thickness of the sediment column above basement underthrust beneath the frontal wedge, from the compilation of Han et al. (2017).

sediments occurs at a stratigraphic level where the pore pressure ratio exceeds the midpoint between the hydrostatic and lithostatic pressures. For comparison, at Nankai accretionary prism abnormal pore pressures below the décollement are indicated by λ^* of 0.4–0.7 (Tsuji et al., 2008). Furthermore, there is a marked along-strike change in the thickness of underthrust sediments near 45°N, with the décollement being 1.4–1.7 km above basement to the south of this latitude (Figure 9c) (Han et al., 2017). Although the height above basement of the layers with $\lambda^* > 0.5$ is not predictive of the amount of underthrust sediment beneath the frontal wedge (Figure 9c), the spatial correlation between these over pressured layers in the lower incoming sediments and a thick underthrust sediment column suggests that the presence of these layers favors the development of a shallow décollement. The fact that we find multiple layers with elevated *Vp*/*Vs* and high pore pressure and in some instances at the same location (e.g., OBS Sites 02, 04, 05, and 06, Figures 6, 9b, and 9c) indicates that there are several stratigraphic levels conducive to the development of the proto-décollement and décollement and that subtle changes (in time and/or space) in strength that favor one horizon over another may be responsible for the documented step up and down within the sediment column of these interfaces (MacKay, 1995). North of 45°N, lower λ^* values correlate with a deeper décollement <0.6 km above basement (Han et al., 2017), perhaps due to a more efficient drainage of fluids from dehydrating deep sediments and oceanic crust.

The northern limit of the region where layers with elevated pore pressures are found ($\lambda^* > 0.5$) also coincides with a transition from landward-vergent thrusting north of ~45°N to seaward-vergent thrusting to the south (MacKay, 1995). Thus, our results also bear on the origin of variations in deformation style along the Cascadia accretionary prism. The spatial correlation between landward vergence off northern Oregon and Washington and the Nitinat and Astoria fans, together with dynamic and frictional modeling of the landward vergent backthrust formation led Adam et al. (2004) to postulate that this uncommon style of wedge deformation is promoted by elevated pore pressures in the basal sediments due to rapid deposition of fan deposits during the glacial age. This hypothesis would imply that estimates of pore pressure (from *Vp*/*Vs*, for example) in the deep sediments are more elevated in the landward vergent region than south of ~45°N where deformation is seaward vergent (e.g., Gutscher et al., 2001; MacKay, 1995). The high-*Vp*, overconsolidated deep sediments found offshore Washington do not support this hypothesis (Han et al., 2017), neither do our results. If anything, we find the opposite pattern, with layers of elevated *Vp*/*Vs* (and inferred high pore pressure) more prevalent where deformation is seaward vergent (Figure 9b). This suggests that factors such as low shear strength at the décollement (e.g., Seely, 1977) and/or a mechanically strong wedge (e.g., MacKay, 1995) resulting from sediment overconsolidation (Han et al., 2017) may be more important controls on wedge deformation than rapid loading of climate-driven sediment flux (Adam et al., 2004; Gutscher et al., 2001).

6. Conclusions

From our modeling of the *Vp*/*Vs* structure of Cascadia Basin sediments we conclude the following:

1. Measurements of average *Vp*/*Vs* above basement (γ_{avg}) and interval *Vp*/*Vs* functions (γ) for Cascadia Basin sediments form well-defined compaction trends as function of depth Z that can be described by $_{avg} = 10.36e^{-2.96\ Z[km]} + 3.03$ and by $\gamma = 6.658e^{-7.326\ Z[km]} + 2.741e^{-0.094\ Z[km]}$, respectively.
2. Between ~8–25 km seaward from the deformation front, *Vp*/*Vs* structure offshore central Oregon is more variable and includes middle-to-deep sediment layers of anomalous *Vp*/*Vs* values, while offshore northern Oregon and Washington *Vp*/*Vs* structure of incoming sediments is more homogeneous and shows little variability along strike.
3. Incoming sedimentary layers with elevated *Vp*/*Vs* could be explained by layers with higher sand content intercalated within a more clayey sedimentary sequence, by layers with higher content of coarser-grained clay minerals relative to finer-grained smectite, and/or by elevated pore fluid pressures. We do not favor the two former interpretations because we would expect them to result in more laterally continuous layers of anomalous *Vp*/*Vs*, contrary to our observations of heterogeneous structure. Instead, we find that predicted normalized pore pressure ratio (λ^*) values above 0.5 correlate spatially with previously reported indicators of sediment underconsolidation. Thus, we interpret that excess pore pressure is a more likely dominant factor in producing anomalously high *Vp*/*Vs* values within the lower half of the incoming sediment section.

4. The proto-décollement offshore central Oregon develops within the incoming sediments at a low-permeability boundary that traps fluids in a stratigraphic level where pore pressure ratio exceeds the midpoint between the hydrostatic and lithostatic values. In contrast, the more normal *Vp*/*Vs* structure further north suggests more efficient fluid drainage from the sediments prior to being accreted to the margin that favors décollement development at or just above the basaltic basement.
5. Incoming sediments off central Oregon and Washington do not show evidence for elevated *Vp*/*Vs* (and thus high pore fluid pressure), thus suggesting that a weak basal sediment layer is not the major factor controlling landward vergence in this region, contrary to previous interpretations.
6. Future drilling of deep sediments at some selected locations along the Cascadia margin could provide the necessary samples and in situ measurements to establish a robust correlation between *Vp*/*Vs* structures derived from OBS data and porosity, composition, and fluid pressures.

Appendix A

We calculate the *Vp*/*Vs* ratio of two end-member clay minerals, fine-grained smectite, and coarse-grain kaolinite, following Mondol et al.'s (2008) empirical relationships describing clay-mineral elastic constants as a function of porosity derived from laboratory measurements made on brine-saturated smectite and kaolinite aggregates:

$$\begin{aligned} K&=a_1\phi^2+a_2\phi+a_3,\\ \mu&=b_1\phi^2+b_2\phi+b_3, \end{aligned} \tag{A1}$$

where K and μ are bulk and shear moduli (in GPa), respectively, ϕ is porosity (in %), coefficients a_i are [0.0055, −0.56, 17.76] and [0.0065, −0.81, 29.03] for kaolinite and smectite, respectively, and coefficients b_i are [0.0026, −0.21, 4.64] and [0.0025, −0.28, 7.92] for kaolinite and smectite, respectively.

The *Vp*/*Vs* ratio as a function of porosity can then be expressed as in terms of $K(\phi)$ and $\mu(\phi)$ as follows:

$$Vp/Vs=\sqrt{\frac{K}{\mu}+\frac{4}{3}}. \tag{A2}$$

The derived *Vp*/*Vs* ratio as a function of porosity (Equation A2) is shown in Figure 8b for both, kaolinite and smectite.

Acknowledgments

This research was funded by National Science Foundation (NSF) Grant OCE-1657237 to J. P. C, OCE-1657839 to A. F. A. and S. H., and OCE-1657737 to S. M. C. Data used in this study were acquired with funding from NSF Grants OCE-1029305 and OCE-1249353. Data used in this research were provided by instruments from the Ocean Bottom Seismic Instrument Center (http://obsic.whoi.edu, formerly OBSIP), which is funded by the NSF. OBSIC/OBSIP data are archived at the IRIS Data Management Center (http://www.iris.edu) under network code X6 (https://doi.org/10.7914/SN/X6_2012). Data processing was conducted with Emerson-Paradigm Software package *Echos* licensed to Woods Hole Oceanographic Institution under Paradigm Academic Software Program and MATLAB package *SeismicLab* of the University of Alberta, Canada (http://seismic-lab.physics.ualberta.ca), under GNU General Public License (MATLAB® is a registered trademark of MathWorks).

References

Adam, J., Klaeschen, D., Kukowski, N., & Flueh, E. R. (2004). Upward delamination of Cascadia Basin sediment infill with landward frontal accretion thrusting caused by rapid glacial age material flux. *Tectonics*, *23*, TC3009. https://doi.org/10.1029/2002TC001475

Anderson, P. N., Duennebier, F. K., & Cessaro, R. K. (1987). Ocean borehole horizontal seismic sensor orientation determined from explosive charges. *Journal of Geophysical Research*, *92*(B5), 3573–3579. https://doi.org/10.1029/JB092iB05p03573

Arnulf, A. F., Harding, A. J., Kent, G. M., Carbotte, S. M., Canales, J. P., & Nedimović, M. R. (2014). Anatomy of an active submarine volcano. *Geology*, *42*, 655–658.

Arnulf, A. F., Harding, A. J., Kent, G. M., & Wilcock, W. S. D. (2018). Structure, seismicity, and accretionary processes at the hot spot-influenced axial seamount on the Juan de Fuca ridge. *Journal of Geophysical Research: Solid Earth*, *123*, 4618–4646. https://doi.org/10.1029/2017JB015131

Arnulf, A. F., Singh, S. C., Harding, A. J., Kent, G. M., & Crawford, W. C. (2011). Strong seismic heterogeneity in layer 2A near hydrothermal vents at the mid-Atlantic ridge. *Geophysical Research Letters*, *38*, L13320. https://doi.org/10.1029/2011GL047753

Atwater, B. F. (1987). Evidence for great Holocene earthquakes along the outer coast of Washington state. *Science*, *236*(4804), 942–944. https://doi.org/10.1126/science.236.4804.942

Atwater, B. F., & Hemphill-Haley, E. (1997). Recurrence intervals for great earthquakes of the past 3,500 years at northeastern Willapa Bay, Washington, Rep., U.S. Geological Survey. https://doi.org/10.3133/pp1576

Atwater, T. (1970). Implications of plate tectonics for the Cenozoic tectonic evolution of western North America. *Geological Society of America Bulletin*, *81*(12), 3513–3536. https://doi.org/10.1130/0016-7606(1970)81[3513:IOPTFT]2.0.CO;2

Au, D., & Clowes, R. M. (1984). Shear-wave velocity of the oceanic lithosphere from ocean bottom seismometer studies. *Geophysical Journal of the Royal Astronomical Society*, *77*(1), 105–123. https://doi.org/10.1111/j.1365-246X.1984.tb01927.x

Bell, S. W., Ruan, Y., & Forsyth, D. W. (2015). Shear velocity structure of abyssal plain sediments in Cascadia. *Seismological Research Letters*, *86*(5), 1247–1252. https://doi.org/10.1785/0220150101

Berryhill, J. R. (1984). Wave-equation datuming before stack. *Geophysics*, *49*(11), 2064–2066. https://doi.org/10.1190/1.1441620

Blangy, J. P., Strandenes, S., Moos, D., & Nur, A. (1993). Ultrasonic velocities in sands—Revisited. *Geophysics*, *58*(3), 344–356. https://doi.org/10.1190/1.1443418

Booth-Rea, G., Klaeschen, D., Grevemeyer, I., & Reston, T. (2008). Heterogeneous deformation in the Cascadia convergent margin and its relation to thermal gradient (Washington, NW USA). *Tectonics*, *27*, TC4005. https://doi.org/10.1029/2007TC002209

Bryant, W. R. (2003). Permeability of clays, silty-clays and clayey-silts. In E. D. Scott, A. H. Bouma, & W. R. Bryant (Eds.), *Siltstones, mudstones and shales: Depositional processes and characteristics* (chap. 8, pp. 344–403). Tulsa, OK: SEPM Society for Sedimentary Geology.

Canales, J. P., & Carbotte, S. (2012). Evolution and hydration of the Juan de Fuca crust and uppermost mantle. https://doi.org/10.7914/SN/X6_2012

Canales, J. P., Carbotte, S. M., Nedimović, M. R., & Carton, H. (2017). Dry Juan de Fuca slab revealed by quantification of water entering Cascadia subduction zone. *Nature Geoscience*, *10*(11), 864–870. https://doi.org/10.1038/ngeo3050

Carbotte, S. M., Canales, J. P., Carton, H., & Nedimović, M. R. (2014). Multi-channel seismic shot data from the Cascadia subduction zone acquired during the R/V Marcus Langseth expedition MGL1211 (2012), *Integrated Earth Data Applications (IEDA)*. https://doi.org/10.1594/IEDA/319000

Carson, B., Yuan, J., Myers, P. B. Jr., & Barnard, W. D. (1974). Initial deep-sea sediment deformation at the base of the Washington continental slope: A response to subduction. *Geology*, *2*(11), 561–564. https://doi.org/10.1130/0091-7613(1974)2%3C561:idsdat%3E2.0.co;2

Castagna, J. P., Batzle, M. L., & Eastwood, R. L. (1985). Relationships between compressional-wave and shear-wave velocities in clastic silicate rocks. *Geophysics*, *50*(4), 571–581. https://doi.org/10.1190/1.1441933

Cochrane, G. R., Moore, J. C., MacKay, M. E., & Moore, G. F. (1994). Velocity and inferred porosity model of the Oregon accretionary prism from multichannel seismic reflection data: Implications on sediment dewatering and overpressure. *Journal of Geophysical Research*, *99*(B4), 7033–7043. https://doi.org/10.1029/93JB03206

Contreras-Reyes, E., Grevemeyer, I., Flueh, E. R., Scherwath, M., & Bialas, J. (2008). Effect of trench-outer rise bending-related faulting on seismic Poisson's ratio and mantle anisotropy: A case study offshore of Southern Central Chile. *Geophysical Journal International*, *173*(1), 142–156. https://doi.org/10.1111/j.1365-246X.2008.03716.x

Dash, R., & Spence, G. (2011). P-wave and S-wave velocity structure of northern Cascadia margin gas hydrates. *Geophysical Journal International*, *187*(3), 1363–1377. https://doi.org/10.1111/j.1365-246X.2011.05215.x

Davis, E. E., Chapman, D. S., Mottl, M. J., Bentkowski, W. J., Dadey, K., Forster, C., et al. (1992). FlankFlux: An experiment to study the nature of hydrothermal circulation in young oceanic crust. *Canadian Journal of Earth Sciences*, *29*(5), 925–952. https://doi.org/10.1139/e92-078

Davis, E. E., & Hyndman, R. D. (1989). Accretion and recent deformation of sediments along the northern Cascadia subduction zone. *Geological Society of America Bulletin*, *101*(11), 1465–1480. https://doi.org/10.1130/0016-7606(1989)101%3C1465:AARDOS%3E2.3.CO;2

Dean, S. M., McNeill, L. C., Henstock, T. J., Bull, J. M., Gulick, S. P. S., Austin, J. A., et al. (2010). Contrasting décollement and prism properties over the Sumatra 2004–2005 earthquake rupture boundary. *Science*, *329*(5988), 207–210. https://doi.org/10.1126/science.1189373

Duennebier, F. K., Anderson, P. N., & Fryer, G. J. (1987). Azimuth determination of and from horizontal ocean bottom seismic sensors. *Journal of Geophysical Research*, *92*(B5), 3567–3572. https://doi.org/10.1029/JB092iB05p03567

Dutta, T., Mavko, G., Mukerji, T., & Lane, T. (2009). Compaction trends for shale and clean sandstone in shallow sediments, Gulf of Mexico. *The Leading Edge*, *28*(5), 590–596. https://doi.org/10.1190/1.3124935

Dvorkin, J., Mavko, G., & Nur, A. (1999). Overpressure detection from compressional- and shear-wave data. *Geophysical Research Letters*, *26*(22), 3417–3420. https://doi.org/10.1029/1999GL008382

Eccles, J. D., White, R. S., & Christie, P. A. F. (2009). Identification and inversion of converted shear waves: Case studies from the European North Atlantic continental margins. *Geophysical Journal International*, *179*(1), 381–400. https://doi.org/10.1111/j.1365-246X.2009.04290.x

Fisher, A. T., & Davis, E. E. (1997). An introduction to the scientific results of Leg 168. In A. T. Fisher, E. E. Davis, & C. Escutia (Eds.), *Proc. ODP, sci. results*, (pp. 3–5). College Station, TX: Ocean Drilling Program.

Flueh, E. R., Fisher, M. A., Bialas, J., Childs, J. R., Klaeschen, D., Kukowski, N., et al. (1998). New seismic images of the Cascadia subduction zone from cruise SO108-ORWELL. *Tectonophysics*, *293*(1-2), 69–84. https://doi.org/10.1016/S0040-1951(98)00091-2

Fujie, G., Kodaira, S., Yamashita, M., Sato, T., Takahashi, T., & Takahashi, N. (2013). Systematic changes in the incoming plate structure at the Kuril trench. *Geophysical Research Letters*, *40*, 88–93. https://doi.org/10.1029/2012GL054340

Geersen, J., McNeill, L., & Henstock, T. J. (2013). The 2004 Aceh-Andaman earthquake: Early clay dehydration controls shallow seismic rupture. *Geochemistry, Geophysics, Geosystems*, *14*, 3315–3323. https://doi.org/10.1002/ggge.20193

Goldfinger, C., Galer, S., Beeson, J., Hamilton, J., Hamilton, T., Black, B., et al. (2017). The importance of site selection, sediment supply, and hydrodynamics: A case study of submarine paleoseismology on the northern Cascadia margin, Washington USA. *Marine Geology*, *384*, 4–46. https://doi.org/10.1016/j.margeo.2016.06.008

Goldfinger, C., Kulm, L. D., Yeats, R. S., Applegate, T. B., MacKay, M. E., & Cochrane, G. R. (1991). Active strike-slip faulting and folding of the Cascadia plate boundary and forearc in central and northern Oregon, *Rep*., U.S. Geological survey, https://doi.org/10.3133/ofr91441S.

Goldfinger, C., Kulm, L. D., Yeats, R. S., Applegate, T. B., MacKay, M. E., & Moore, G. F. (1992). Transverse structural trends along the Oregon convergent margin: Implications for Cascadia earthquake potential and crustal rotations. *Geology*, *20*(2), 141–144.

Goldfinger, C., Nelson, C. H., & Johnson, J. E. (2003). Holocene earthquake records from the Cascadia subduction zone and northern San Andreas Fault based on precise dating of offshore turbidites. *Annual Review of Earth and Planetary Sciences*, *31*(1), 555–577. https://doi.org/10.1146/annurev.earth.31.100901.141246

Goldfinger, C., Nelson, H. C., Morey, A. E., Johnson, J. E., Patton, J. R., Karabanov, E., et al. (2012). Turbidite event history—Methods and implications for Holocene paleoseismicity of the Cascadia subduction zone, Rep., USGS Professional Paper 1661-F, 170 pp.

Griggs, G. B., & Kulm, L. D. (1970). Sedimentation in Cascadia deep-sea channel. *GSA Bulletin*, *81*(5), 1361–1384. https://doi.org/10.1130/0016-7606(1970)81[1361:SICDC]2.0.CO;2

Gulick, S. P. S., Austin, J. A., McNeill, L., Bangs, N. L. B., Martin, K. M., Henstock, T. J., et al. (2011). Updip rupture of the 2004 Sumatra earthquake extended by thick indurated sediments. *Nature Geoscience*, *4*(7), 453–456. https://doi.org/10.1038/NGEO1176

Gulick, S. P. S., Meltzer, A. M., & Clarke, S. H. (1998). Seismic structure of the southern Cascadia subduction zone and accretionary prism north of the Mendocino triple junction. *Journal of Geophysical Research*, *103*(B11), 27,207–27,222. https://doi.org/10.1029/98JB02526

Gutscher, M.-A., Klaeschen, D., Flueh, E. R., & Malaivieille, J. (2001). Non-coulomb wedges, wrong-way thrusting, and natural hazards in Cascadia. *Geology*, *29*(5), 379–382. https://doi.org/10.1130/0091-7613(2001)029%3C0379:NCWWWT%3E2.0.CO;2

Han, D.-H., Nur, A., & Morgan, D. (1986). Effects of porosity and clay content on wave velocities in sandstones. *Geophysics*, *51*(11), 2093–2107. https://doi.org/10.1190/1.1442062

Han, S., Bangs, N. L., Carbotte, S. M., Saffer, D. M., & Gibson, J. C. (2017). Links between sediment consolidation and Cascadia megathrust slip behaviour. *Nature Geoscience*, *10*(12), 954–959. https://doi.org/10.1038/s41561-017-0007-2

Han, S., Carbotte, S. M., Canales, J. P., Carton, H., Nedimović, M. R., Gibson, J., & Horning, G. (2016). Seismic reflection imaging of the Juan de Fuca plate from ridge to trench; new constraints on the distribution of faulting and evolution of the crust prior to subduction. *Journal of Geophysical Research: Solid Earth*, *121*, 1849–1872. https://doi.org/10.1002/2015JB012416

Han, S., Carbotte, S. M., Canales, J. P., Nedimović, M. R., & Carton, H. (2018). Along-trench structural variations of the subducting Juan de Fuca plate from multichannel seismic reflection imaging. *Journal of Geophysical Research: Solid Earth*, *123*, 3122–3146. https://doi.org/10.1002/2017JB015059

Harding, A. J., Kent, G. M., Blackman, D. K., Singh, S., & Canales, J. P. (2007). A new method for MCS refraction data analysis of the uppermost section at a mid-Atlantic ridge core complex, *Eos Trans. AGU*, *88*(52), fall meet. Suppl., Abstract S12A-03.

Heuret, A., Conrad, C. P., Funiciello, R., Lallemand, S., & Sandri, L. (2012). Relation between subduction megathrust earthquakes, trench sediment thickness and upper plate strain. *Geophysical Research Letters*, *39*, L05304. https://doi.org/10.1029/2011GL050712

Horning, G., Canales, J. P., Carbotte, S. M., Han, S., Carton, H., Nedimović, M. R., & van Keken, P. E. (2016). A 2-D tomographic model of the Juan de Fuca plate from accretion at axial seamount to subduction at the Cascadia margin from an active source OBS survey. *Journal of Geophysical Research: Solid Earth*, *121*, 5859–5879. https://doi.org/10.1002/2016JB013228

Huffman, A. R., & Castagna, J. P. (2001). The petrophysical basis for shallow-water flow prediction using multicomponent seismic data. *The Leading Edge*, *20*(9), 1030–1052. https://doi.org/10.1190/1.1487308

Hüpers, A., Torres, M. E., Owari, S., McNeill, L. C., Dugan, B., Henstock, T. J., et al. (2017). Release of mineral-bound water prior to subduction tied to shallow seismogenic slip off Sumatra. *Science*, *356*(6340), 841–844. https://doi.org/10.1126/sceince.aal3429

Hyndman, R. D., Moore, G. F., & Moran, K. (1993). Velocity, porosity, and pore-fluid loss from the Nankai subduction zone accretionary prism. In I. A. Hill, A. Taira, J. V. Firth, et al. (Eds.), *Proceedings of the ocean drilling program, scientific results*, (pp. 211–220). College Station, TX: Ocean Drilling Program.

Hyndman, R. D., Yorath, C. J., Clowes, R. M., & Davis, E. E. (1990). The northern Cascadia subduction zone at Vancouver Island: Seismic structure and tectonic history. *Canadian Journal of Earth Sciences*, *27*(3), 313–329. https://doi.org/10.1139/e90-030

Johnson, H. P., Hautala, S. L., & Bjorklund, T. A. (2012). The thermal environment of Cascadia Basin. *Geochemistry, Geophysics, Geosystems*, *13*, Q07003. https://doi.org/10.1029/2011GC003922

Karlin, R. (1980). Sediment sources and clay mineral distributions off the Oregon coast. *Journal of Sedimentary Research*, *50*(2), 543–559. https://doi.org/10.1306/212f7a4a-2b24-11d7-8648000102c1865d

Katahara, K. W. (1996). Clay mineral elastic properties, in *SEG Technical Program Expanded Abstracts 1996*, edited, pp. 1691-1694.

Lee, M. W. (2003). Elastic properties of overpressured and unconsolidated sediments, U. S Geological Survey Bulletin, 2214.

MacKay, M. E. (1995). Structural variation and landward vergence at the toe of the Oregon prism. *Tectonics*, *14*(6), 1309–1320. https://doi.org/10.1029/95TC02320

MacKay, M. E., Moore, G. F., Cochrane, G. R., Casey Moore, J., & Kulm, L. D. (1992). Landward vergence and oblique structural trends in the Oregon margin accretionary prism: Implications and effect on fluid flow. *Earth and Planetary Science Letters*, *109*(3-4), 477–491. https://doi.org/10.1016/0012-821X(92)90108-8

McCrory, P. A., Blair, J. L., Waldhauser, F., & Oppenheimer, D. H. (2012). Juan de Fuca slab geometry and its relation to Wadati-Benioff zone seismicity. *Journal of Geophysical Research*, *117*, B09306. https://doi.org/10.1029/2012JB009407

McNeill, L. C., Goldfinger, C., Kulm, L. D., & Yeats, R. S. (2000). Tectonics of the Neogene Cascadia forearc basin: Investigations of a deformed Late Miocene unconformity. *Geological Society of America Bulletin*, *112*(8), 1209–1224. https://doi.org/10.1130/0016-7606(2000)112%3C1209:TOTNCF%3E2.0.CO;2

Mondol, N. H., Jahren, J., Bjorlykke, K., & Brevik, I. (2008). Elastic properties of clay minerals. *The Leading Edge*, *27*(6), 758–770. https://doi.org/10.1190/1.2944161

Nedimović, M. R., Carbotte, S. M., Diebold, J. B., Harding, A. J., Canales, J. P., & Kent, G. M. (2008). Upper crustal evolution across the Juan de Fuca ridge flanks. *Geochemistry, Geophysics, Geosystems*, *9*, Q09006. https://doi.org/10.1029/2008GC002085

Peacock, S., & Westbrook, G. K. (2000). Shear wave velocities and anisotropy in the Barbados accretionary complex. *Journal of Geophysical Research*, *105*(B12), 28,489–28,508. https://doi.org/10.1029/2000JB900350

Peacock, S., Westbrook, G. K., & Bais, G. (2010). S-wave velocities and anisotropy in sediments entering the Nankai subduction zone, offshore Japan. *Geophysical Journal International*, *180*, 743–758.

Prasad, M. (2002). Acoustic measurements in unconsolidated sands at low effective pressure and overpressure detection. *Geophysics*, *67*(2), 405–412. https://doi.org/10.1190/1.1468600

Scholl, D. W., Kirby, S. H., von Huene, R., Ryan, H., Wells, R. E., & Geist, E. L. (2015). Great (≥Mw8.0) megathrust earthquakes and the subduction of excess sediment and bathymetrically smooth seafloor. *Geosphere*, *11*(2), 236–265. https://doi.org/10.1130/GES01079.1

Seely, D. R. (1977). The significance of landward vergence and oblique structural trends on trench inner slopes. In M. Talwani, & W. C. Pitman (Eds.), *Island arcs, deep sea trenches and back-arc basins* (chap. 15, pp. 187–198). Washington, D.C: American Geophysical Union.

Seno, T. (2017). Subducted sediment thickness and Mw 9 earthquakes. *Journal of Geophysical Research: Solid Earth*, *122*, 470–491. https://doi.org/10.1002/2016JB013048

Shi, Y., & Wang, C.-Y. (1988). Generation of high pore pressures in accretionary prisms: Inferences from the Barbados subduction complex. *Journal of Geophysical Research*, *93*(B8), 8893–8910. https://doi.org/10.1029/JB093iB08p08893

Shipboard Scientific Party (1973). Site 174. In L. D. Kulm, R. von Huene, et al. (Eds.), *Initial reports of the deep sea drilling project* (pp. 97–167). Washington: U.S. Goverment Printing Office.

Shipboard Scientific Party (1994). Site 888. In G. K. Westbrook, B. Carson, R. J. Musgrave, et al. (Eds.), *Proceedings of the ocean drilling program, initial reports* (pp. 55–125). College Station, TX: Ocean Drilling Program.

Shipboard Scientific Party (1997a). Rough basement transect (sites 1026 and 1027). In E. E. Davis, A. T. Fisher, J. V. Firth, et al. (Eds.), *Proceedings of the ocean drilling program, initial reports* (pp. 101–160). College Station, TX: Ocean Drilling Program.

Shipboard Scientific Party (1997b). Introduction and summary: Hydrothermal circulation in the oceanic crust and its consequences on the eastern flank of the Juan de Fuca ridge. In E. E. Davis, A. T. Fisher, J. V. Firth, et al. (Eds.), *Proceedings of the ocean drilling program initial results* (pp. 7–21). College Station, TX: Ocean Drilling Program.

Shipboard Scientific Party (2003). Leg 204 summary. In *Proc. ODP, initi. repts* (Vol. 204, pp. 1–75). College Station, TX: Ocean Drilling Program.

Silver, E. A. (1972). Pleistocene tectonic accretion of the continental slope off Washington. *Marine Geology*, *13*(4), 239–249. https://doi.org/10.1016/0025-3227(72)90053-9

Skarbek, R. M., & Saffer, D. M. (2009). Pore pressure development beneath the décollement at the Nankai subduction zone: Implications for plate boundary fault strength and sediment dewatering. *Journal of Geophysical Research*, *114*, B07401. https://doi.org/10.1029/2008JB006205

Spence, G. D., Hyndman, R. D., Davis, E. E., & Yorath, C. J. (2001). Seismic structure of the northern Cascadia accretionary prism: Evidence from new multichannel seismic reflection data. In R. Meissner, L. Brown, H.-J. Dürbaum, W. Franke, K. Fuchs, & F. Seifert (Eds.), *Continental lithosphere: Deep seismic reflections*, (pp. 257–263). Washington, D.C.: American Geophysical Union.

Spudich, P., & Orcutt, J. A. (1980). Petrology and porosity of an oceanic crustal site: Results from wave form modeling of seismic refraction data. *Journal of Geophysical Research*, *85*(B3), 1409–1433. https://doi.org/10.1029/JB085iB03p01409

Stewart, R. R., Gaiser, J. E., Brown, R. J., & Lawton, D. C. (2003). Converted-wave seismic exploration: Applications. *Geophysics*, *68*(1), 40–57. https://doi.org/10.1190/1.1543193

Tessmer, G., & Behle, A. (1988). Common reflection point data-stacking technique for converted waves. *Geophysical Prospecting*, *36*(7), 671–688. https://doi.org/10.1111/j.1365-2478.1988.tb02186.x

Thomsen, L. (1999). Converted-wave reflection seismology over inhomogeneous, anisotropic media. *Geophysics*, *64*(3), 678–690. https://doi.org/10.1190/1.1444577

Tréhu, A. M., Braunmiller, J., & Davis, E. (2015). Seismicity of the Central Cascadia continental margin near 44.5°N: A decadal view. *Seismological Research Letters*, *86*(3), 819–829. https://doi.org/10.1785/0220140207

Tréhu, A. M., Braunmiller, J., & Nabelek, J. L. (2008). Probable low-angle thrust earthquakes on the Juan de Fuca—North America plate boundary. *Geology*, *36*(2), 127–130. https://doi.org/10.1130/g24145a.1

Tsuji, T., Dvorkin, J., Mavko, G., Nakata, N., Matsuoka, T., Nakanishi, A., et al. (2011). Vp/Vs ratio and shear-wave splitting in the Nankai trough seismogenic zone: Insights into effective stress, pore pressure, and sediment consolidation. *Geophysics*, *76*(3), WA71–WA82. https://doi.org/10.1190/1.3560018

Tsuji, T., Kamei, R., & Pratt, R. G. (2014). Pore pressure distribution of a mega-splay fault system in the Nankai trough subduction zone: Insight into up-dip extent of the seismogenic zone. *Earth and Planetary Science Letters*, *396*, 165–178.

Tsuji, T., Tokuyama, H., Costa Pisani, P., & Moore, G. (2008). Effective stress and pore pressure in the Nankai accretionary prism off the Muroto Peninsula, southwestern Japan. *Journal of Geophysical Research*, *113*, B11401. https://doi.org/10.1029/2007JB005002

Underwood, M. B. (2002). Strike-parallel variations in clay minerals and fault vergence in the Cascadia subduction zone. *Geology*, *30*(2), 155–158. https://doi.org/10.1130/0091-7613(2002)030%3C0155:SPVICM%3E2.0.CO;2

Underwood, M. B., & Hoke, K. D. (2000). Composition and provenance of turbidite sand and hemipelagic mud in northwestern Cascadia Basin. In A. Fisher, E. E. Davis, & C. Escutia (Eds.), *Proc. ODP, sci. results*, (pp. 51–65). College Station, TX: Ocean Drilling Program.

Underwood, M. B., Hoke, K. D., Fisher, A. T., Davis, E. E., Giambalvo, E., Zühlsdorff, L., & Spinelli, G. (2005). Provenance, stratigraphic architecture, and hydrogeologic influence of turbidites on the mid-ocean ridge flank of northwestern Cascadia Basin, Pacific Ocean. *Journal of Sedimentary Research*, *75*(1), 149–164. https://doi.org/10.2110/jsr.2005.012

van Rijsingen, E., Lallemand, S., Peyret, M., Arcay, D., Heuret, A., Funiciello, F., & Corbi, F. (2018). How subduction interface roughness influences the occurrence of large interplate earthquakes. *Geochemistry, Geophysics, Geosystems*, *19*, 2342–2370. https://doi.org/10.1029/2018GC007618

Vannucchi, P., Spagnuolo, E., Aretusini, S., Di Toro, G., Ujiie, K., Tsutsumi, A., & Nielsen, S. (2017). Past seismic slip-to-trench recorded in Central America megathrust. *Nature Geoscience*, *10*(12), 935–940. https://doi.org/10.1038/s41561-017-0013-4

Vanorio, T., Prasad, M., & Nur, A. (2003). Elastic properties of dry clay mineral aggregates, suspensions and sandstones. *Geophysical Journal International*, *155*, 319–326.

Wang, Z., Wang, H., & Cates, M. E. (2001). Effective elastic properties of solid clays. *Geophysics*, *66*(2), 428–440. https://doi.org/10.1190/1.1444934

Westbrook, G., Carson, B., & Shipboard Scientific Party (1994). Summary of Cascadia drilling results. In G. Westbrook, B. Carson, R. J. Musgrave, et al. (Eds.), *Proceedings of the ocean drilling program, initial reports*, (pp. 389–396). College Station, TX: Ocean Drilling Program.

Westbrook, G. K., Chand, S., Rossi, G., Long, C., Bünz, S., Camerlenghi, A., et al. (2008). Estimation of gas hydrate concentration from multi-component seismic data at sites on the continental margins of NW Svalbard and the Storegga region of Norway. *Marine and Petroleum Geology*, *25*(8), 744–758. https://doi.org/10.1016/j.marpetgeo.2008.02.003

Wilson, D. S. (2002). The Juan de Fuca plate and slab—Isochron structure and Cenozoic plate motions. In S. Kirby, K. Wang, & S. Dunlop (Eds.), *The Cascadia subduction zone and related subduction systems. Seismic structure, intraslab earthquakes and processes, and earthquake hazards*, (pp. 9–12). U.S. Geol. Survey Open-File Report 02-328. Reston, VA: U.S. Geological Survey.

Yilmaz, Ö. (2001). *Seismic data analysis: Processing, inversion, and interpretation of seismic data* (Vol. 2, second ed., p. 2027). Tulsa, OK: Society of Exploration Geophysicists.

Yuan, T., Spence, G. D., & Hyndman, R. D. (1994). Seismic velocities and inferred porosities in the accretionary wedge sediments at the Cascadia margin. *Journal of Geophysical Research*, *99*(B3), 4413–4427. https://doi.org/10.1029/93JB03203

Zimmer, M., Prasad, M., & Mavko, G. (2002). Pressure and porosity influences on V_P–V_S ratio in unconsolidated sands. *The Leading Edge*, *21*(2), 178–183. https://doi.org/10.1190/1.1452609